Surface & Coatings Technology 505 (2025) 132090

Contents lists available at ScienceDirect

Surface & Coatings Technology

journal homepage: www.elsevier.com/locate/surfcoat

Effect of powder morphology on tribological performance of HVAF-sprayed WC-CoCr coatings

L. Bortolotti [a,*], G. Ruggiero [a], G. Bolelli [a,b,c], L. Lusvarghi [a,b,c], S. Morelli [a], S. Björklund [d], O. Lanz [e], S. Joshi [d]

[a] Department of Engineering "Enzo Ferrari", University of Modena and Reggio Emilia, Via Pietro Vivarelli 10/1, 41125 Modena, Italy
[b] InterMech – MO.RE., Centro Interdipartimentale per la Ricerca Applicata e i Servizi nel Settore della Meccanica Avanzata e della Motoristica, University of Modena and Reggio Emilia, Via Pietro Vivarelli 2, 41125 Modena, Italy
[c] Consorzio Interuniversitario Nazionale per la Scienza e Tecnologia dei Materiali (INSTM), Research Unit: University of Modena and Reggio Emilia, Via Pietro Vivarelli 10/1, 41125 Modena, Italy
[d] University West, Gustava Melins Gata 2, Trollhättan, Sweden
[e] Höganäs Germany GmbH, Säckinger Str. 51, Laufenburg, Germany

ARTICLE INFO

Keywords:
WC-CoCr
High velocity air-fuel (HVAF)
Powder morphology
Sliding wear
Erosion
Deposition efficiency

ABSTRACT

This study investigates the tribological behavior of WC-CoCr coatings deposited using High-Velocity Air Fuel (HVAF) thermal spraying. Three distinct types of feedstock powders were employed to examine the influence of powder morphology on coating performance: a dense, angular fused-and-crushed powder; a spherical, porous agglomerated-and-sintered powder, and a newly developed powder with intermediate features. All powders had analogous particle size distribution approximately in the range of 7–20 μm. Two coating thicknesses were deposited with each powder (50 μm and 150 μm), additionally aiming to verify the possibility of depositing thin hardmetal coatings. The coatings microstructure was characterized, their hardness and porosity were measured and their tribological properties were evaluated by means of ball-on-disk sliding tests and dry jet erosion tests at various impact angles.

The results demonstrated that powder morphology significantly affects deposition efficiency. The newly developed powder offers notable advantages, such as higher deposition efficiency, which accelerates the spraying process and boosts production productivity, along with reduced sensitivity to parameter variations. In fact, the newly developed powder exhibited more consistent deposition rates across varying process conditions. Coatings derived from the new manufacturing route powder also showed improved cohesion and hardness due to stronger interparticle bonding and peening effects. On the other hand, surface roughness was unaffected by the powder type, and the coatings produced from the three powders had comparable wear resistance under erosion and sliding conditions. Coating thickness, rather than powder morphology, appeared to play a greater role in determining wear performance. The thicker coatings demonstrated superior resistance under both test conditions, due to reduced substrate influence.

1. Introduction

Thermal sprayed coatings comprising a combination of tungsten carbide (WC) dispersed within a metallic matrix (Co) have emerged as a remarkable solution for a diverse range of industrial applications. These WC-Co coatings exhibit unique properties, making them highly preferred in various sectors. They are widely used to protect metallic components in automatic machinery, oil and gas equipment, steel-making and papermaking rolls, hydraulic systems, steam turbine blades, and engine valves [1,2]. The primary reason behind their widespread adoption is their ability to provide protection against erosive, abrasive, and other wear-prone environments. To enhance the corrosion and oxidation resistance of WC-Co hardmetals, metallic chromium can be added, resulting in WC-CoCr compositions [3]. Moreover, the addition of Cr promotes the formation of M6C (where M = Co, Cr, W), also known as η-phase which is more stable than a metallic matrix phase, although it may impair ductility and toughness [4]. Another approach is the incorporation of chromium carbide, leading to compositions such as

* Corresponding author.
E-mail address: luca.bortolotti@unimore.it (L. Bortolotti).

https://doi.org/10.1016/j.surfcoat.2025.132090
Received 25 October 2024; Received in revised form 10 January 2025; Accepted 25 March 2025
Available online 26 March 2025

Table 1
Feedstock powders and designations.

Trade name	Designation	Supplier	Designation of the powder	Manufacturing method	Particle size
Amperit® 558.052	P1	Höganäs	WC-CoCr, 86–10-4	Agglomerated & Sintered	-20 + 5 μm
Amperit® 554.067	P2	Höganäs	WC-CoCr, 86–10-4	Sintered & Crushed	−15 + 5 μm
Amperit® 658.067	P3	Höganäs	WC-CoCr, 86–10-4	Agglomerated & Sintered (t-route)	−15 + 5 μm

Table 2
Configuration used for spraying.

Gun Type	Code	Nozzle name	Nozzle length (mm)	Nozzle exit diameter (mm)
M2	N1	3L0F	200	11.8
	N2	3L3F	200	14
M3	N3	4 L2	250	22.8
	N4	4 L4	250	25.4

WC-Cr_3C_2-(Co,Ni) [5,6], or the development of mixed carbide-based compositions like WC-$(W,Cr)_2C$-Ni [7–9].

Various thermal spraying techniques can be employed to produce these coatings, including Atmospheric Plasma Spraying (APS) [10], High Velocity Oxygen Fuel (HVOF) [11,12], and High Velocity Air Fuel (HVAF) [13,14]. Among these techniques, HVOF and HVAF are particularly favoured for depositing WC-Co coatings due to their ability to achieve denser coatings with minimal oxidation compared to plasma sprayed coatings [15]. HVOF and HVAF techniques, indeed, offer lower particle temperature and higher kinetic energy in comparison to processes like plasma spraying. This is beneficial both to improve interparticle cohesion and minimize porosity, and to minimize oxidation, because the metallic binders (such as Co, Ni, or Fe-based alloys) in WC-Co coatings have relatively low melting temperatures, requiring deposition processes that operate at correspondingly moderate temperatures.

This work specifically offers a comprehensive investigation into the deposition efficiency, microstructure, and tribological performance of HVAF-sprayed WC-CoCr coatings obtained with three distinct kinds of feedstock powders. A key benefit of this investigation is to provide a guidance for users to choose the most suitable powder for their specific applications. Indeed, several studies conducted on WC-CoCr coatings have demonstrated that the tribological performances of these coatings can depend on the feedstock powder properties, and deposition parameters employed [13,16,17]. Feedstock powders with the same chemical compositions but obtained through different manufacturing methods can exhibit distinct physical properties [18]. Agglomeration and subsequent sintering of the resulting granules or, conversely, sintering of bulk pellets and subsequent crushing are potential routes for obtaining powders suitable for thermal spraying [19]. The varied morphologies of these powders can influence the quality of the coatings and the cohesion between individual splats, consequently affecting their wear response.

For instance, the irregular morphology of sintered and crushed (S&C) powders reduce their flowability. Poor flowability may result in fluctuations in the powder flow rate, leading to an uneven microstructure of the coating [18]. On the other hand, S&C particles are almost fully dense as they come from fully sintered blocks. These dense particles are usually heated to lower temperatures during spraying [20] (meaning less likelihood of WC dissolution and decarburization), and they also improve coating density by shot-peening effects. Agglomerated & sintered (A&S) powders have a morphology with rather high sphericity which improves flowability compared to S&C powders. However, in contrast to S&C powders, A&S powder particles have a certain degree of retained porosity. This compromises coating density and compressive stress levels.

Research by Bolelli et al. have demonstrated that good inter-lamellae cohesion is a major factor in achieving high abrasive resistance. They also have noted that HVOF and HVAF coatings deposited from coarse feedstock powders experience greater wear loss compared to those obtained from fine powders. This is because weak interparticle cohesion in coarse powders leads to brittle inter-lamellar detachment, resulting in lower fracture toughness [13]. The sliding behavior of HVAF coatings obtained from different hardmetal feedstock powders was investigated by Lyphout et al. They found that the size of WC grains, whether coarse or fine, can result in two distinct wear mechanisms [21]. The use of coarse WC grains leads to localized plastic flow within the carbide grains, causing fracturing and pull-out. On the other hand, when fine carbides are uniformly distributed, the stress distribution becomes more balanced. In this case, plastic flow of the matrix material drives near-surface deformation, pulling out the small WC grains. The primary wear mechanism in this scenario is the gradual pull-out of individual carbide grains. Furthermore, the study highlighted the importance of particle sintering in determining the strength of the coatings. Feedstock powders containing insufficiently sintered fine carbides (low powder strength) resulted in coatings with high decarburization levels and limited cohesive strength, promoting large-scale surface fracturing as an additional wear mechanism [21].

Whilst the previous works focused mainly on the effects of particle size distribution and carbide size, the present one focuses on powders with different morphologies, obtained by distinct manufacturing routes but having approximately the same size distribution and carbide size. As mentioned above, indeed, this can have major effects on the resulting coating quality, but as each powder manufacturing technologies has advantages and disadvantages, predicting the outcome is not straightforward. This work specifically offers a comprehensive investigation into the tribological performance of WC-CoCr HVAF coatings obtained by employing three distinct kinds of feedstock powders.

2. Experimental materials and procedures

2.1. Feedstock materials and coating deposition process

The feedstock materials utilized in this research are presented in Table 1. They are all commercially available thermal spray powders: Amperit® 554.067 (WC-CoCr, 86–10-4, sintered and crushed, −15 + 5 μm) and Amperit® 558.052 (WC-CoCr, 86–10-4, agglomerated and sintered, −20 + 5 μm), and the recently developed Amperit® 658.067 (WC-CoCr, 86–10-4, −15 + 5 μm). For clarity and consistency, the three powders employed in this study will be hereafter referred to as P1, P2 and P3, respectively, as summarized in Table 1. Based on the manufacturer's indications, the P3 powder is intended as a compromise between S&C and A&S powders since its proprietary manufacturing process is meant to result in a mixture of coarser dense particles, which improve flowability and provide shot peening, together with finer dense particles.

The HVAF spraying was conducted at University West, Sweden, utilizing two distinct guns. The M2 HVAF gun (Uniquecoat Technologies LLC, Oilville, VA, USA) with nozzle configurations 3L0F (N1) and 3L3F (N2), as well as the M3 HVAF gun (Uniquecoat Technologies LLC, Oilville, VA, USA) with nozzle configurations 4 L2 (N3) and 4 L4 (N4). The gun configurations are presented in Table 2. All powders were sprayed onto low carbon Domex 355 steel disks with a diameter of 25.4 mm and a thickness of 6 mm, using propane as the fuel and nitrogen as the carrier gas. Based on previous internal trials, no grit-blasting was performed before deposition. The spraying parameters are specified in Table 3, which were determined through preliminary experiments to achieve a

Table 3
Spraying parameters.

Powder label / name	P1 / Amperit® 558.052				P2 / Amperit® 554.067				P3 / Amperit® 658.067			
Torch model	M2		M3		M2		M3		M2		M3	
Nozzle configuration	N1	N2	N3	N4	N1	N2	N3	N4	N1	N2	N3	N4
Air [psi]	93	96	109	105	93	96	109	105	93	96	109	105
Fuel 1 [psi]	90	93	100	110	90	93	100	110	90	93	100	110
Fuel 2 [psi]	–	–	105	105	–	–	105	105	–	–	105	105
Carrier gas [l/min]	40	40	40	40	40	40	40	40	40	40	40	40
Feed rate [g/min]	200	200	200	200	200	200	200	200	200	200	200	200
SoD [mm]	200	200	300	300	200	200	300	300	200	200	300	300
N° of passes (50 μm)	2	4	5	6	2	4	4	5	3	4	3	3.5
N° of passes (150 μm)	6	15	16	–	7	12	12	16	10	11	10	9

Table 4
Designation for all the coatings.

Powder		P1		P2		P3	
Tickness (μm)		50	150	50	150	50	150
M2	**N1**	P1N1–50	P1N1	P2N1–50	P2N1	P3N1–50	P3N1
	N2	P1N2–50	P1N2	P2N2–50	P2N2	P3N2–50	P3N2
M3	**N3**	P1N3–50	P1N3	P2N3–50	P2N3	P3N3–50	P3N3
	N4	P1N4–50		P2N4–50	P2N4	P3N4–50	P3N4

dense microstructure (porosity <1 %) and a satisfactory deposition rate (20–10 μm/pass). The G4 gravimetric feeder (Uniquecoat Technologies LLC) supplied the guns with a powder feed rate of 200 g/min for all the coatings. The powder was injected into the long pre-chamber through a short axial powder injector.

The total number of deposition cycles was determined to achieve coating thicknesses of 50 μm and 150 μm for all the coatings. In this study, all three powders were sprayed using each nozzle configuration, except for Amperit® 558.052, which was not sprayed with nozzle N4 in the run targeting a thickness of 150 μm. Henceforth, the coatings developed using different gun and nozzle configurations, along with the three powders and the targeted thicknesses, will be denoted as indicated in Table 4.

The deposition rate, expressed in terms of thickness per pass (μm/pass), was calculated by measuring the sample's thickness before and after each spray run, employing a digital micrometer with ±0.001 mm accuracy. Additionally, the roughness of the as-deposited coatings (Ra) was assessed using a surface roughness tester (Surftest 301). Five measurements were performed on each coating, and the average values are reported herein.

2.2. Powder characterization

The cross-sections of both powders were prepared by cold mounting in epoxy resin, ground using a 45 μm diamond disk and then polished using 9 μm and 3 μm Kemet diamond slurries, with a final polishing step using a colloidal silica MasterMet 2 suspension and cleaned ultrasonically in ethanol. The microstructures were studied by scanning electron microscopy (SEM: TM3000 tabletop microscope, Hitachi, Japan). Their phase composition was investigated by X-ray diffractometry (X-Pert PRO, PANAlytical, Almelo, NL; Cu-Kα radiation emitted at 40 kV voltage, 40 mA current) conducted over a 25° – 90° 2θ angular range, with a scan step 0.017° and a counting time of 120 s/step. A 1-D array of solid-state detectors (X'Celerator) was employed to measure the intensity of the diffracted beam. The patterns were analyzed using the High Score Plus (PANAlytical) software. The particle size distribution was measured by laser scattering (Mastersizer 2000, Malvern Panalytical, Malvern, UK) using an ultrasound-assisted wet dispersion unit (Hydro-2000 S, Malvern Panalytical).

2.3. Coating characterization

The phase composition of the coatings was characterized by XRD (X'Pert PRO) measurements applying the same acquisition conditions described for the powders. Microstructures and chemical composition of the coatings were investigated by SEM (TM3000) equipped with an Energy Dispersive Spectroscopy system (EDS: Quantax-200, Bruker Nano GmbH, Berlin, Germany) on cross-sections (hot-mounted in Epo-Met™ G resin, Buehler, Lake Bluff, IL, USA) and on polished surfaces (polishing procedure outlined in Section 2.4). The SEM was operated with a 15 keV electron beam energy. Image analysis with the ImageJ software (NIH, Bethesda, MD, USA) was used to evaluate the actual thickness of the coatings on 5 cross-section SEM micrographs collected at 800× and 1500× magnification.

The micro-hardness of the coatings was assessed on polished cross-sections by Vickers micro-indentation (Duramin-40, Struers, Germany), using 2.942 N maximum load, 10 s holding time at maximum load following the ASTM E384 standard [1]. Ten indentations were performed on each sample.

2.4. Ball-on-disk sliding test

Unidirectional dry sliding wear tests were performed in a tribometer (Tribometer TRB3, Anton-Paar, Switzerland) having a ball-on-disc configuration according to ASTM G99 [2]. Prior to testing, all samples were ground using 165/125/70/45 μm diamond disks and polished using 9 μm and 3 μm Kemet diamond slurries, with a final polishing step using a colloidal silica MasterMet 2 suspension, achieving a final roughness Ra < 0.2 μm. Sample were then cleaned with ethanol in an ultrasonic bath. The polished samples were fixed to the rotating plate of the tribometer. Sintered α-Al_2O_3 balls (manufacturer's nominal hardness: 19 GPa) of 6 mm diameter were pressed against them by a normal load $P = 20$ N.

Tests were performed in air at room temperature ($T = 25 \pm 2$ °C, R. H. = 55 ± 2 %). In all cases, the overall sliding distance was 5000 m; at least three repetitions were performed for each test on wear traces with radii of 6, 7, and 9 mm. Tests were carried out with a relative sliding speed (v) of 0.2 m/s, resulting in a duration of 6 h 56 min. It is noted that the use of different radii in the ball-on-disc tests, while maintaining the same total sliding distance, resulted in variations in cycle count that might cause increased data scatter. Due to limited sample availability,

Table 5
Parameters of the dry erosion test.

Nominal coating thickness	150 μm	50 μm
Abrasive particle velocity	70 m/s	70 m/s
Impingement angle	30°, 60° and 90°	30° and 90°
Discharge feed rate	2 g/min	2 g/min
Stand-off distance	10 mm	10 mm
Time	3 min	1 min

tests under identical conditions for all radii were not feasible.

The friction coefficient was monitored using a load cell attached to the ball-holding arm. The specific wear rate of the sample, expressed as volume loss per unit sliding distance and unit normal load, was assessed by measuring the wear track volume using a white light interferometry (WLI) technique (Profilm 3D, Filmetrics, Unterhaching, Germany). Specifically, profiles were acquired at four different locations across the wear track and the average cross-sectional track area (A) was computed. The track volume (V) was obtained as the product of the cross-sectional area multiplied by the track length $V = A \bullet (\pi d)$ and was converted to volumetric specific wear rate (W) as $W = V/(Ps)$.

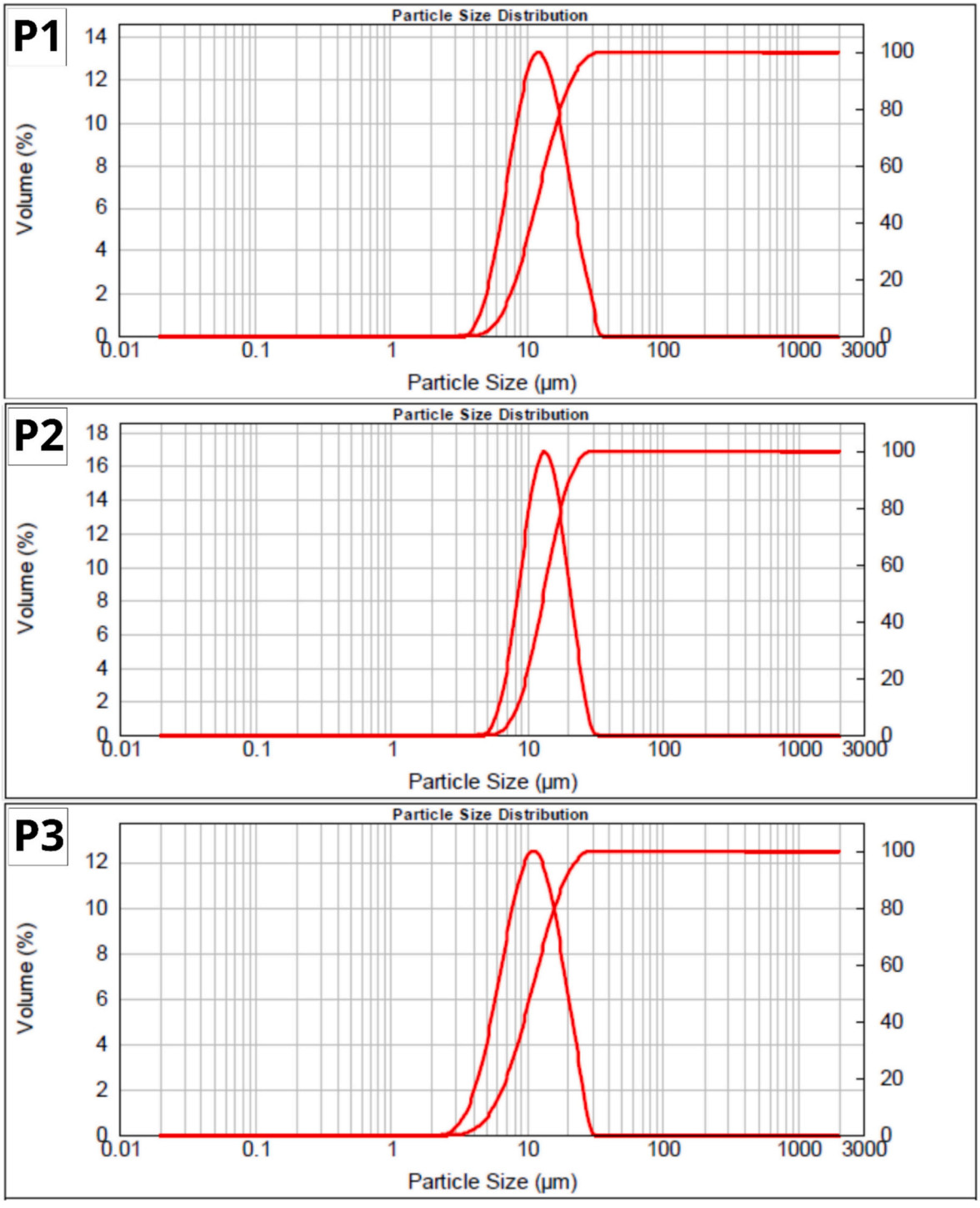

Fig. 1. Particle size distribution of the feedstock powders.

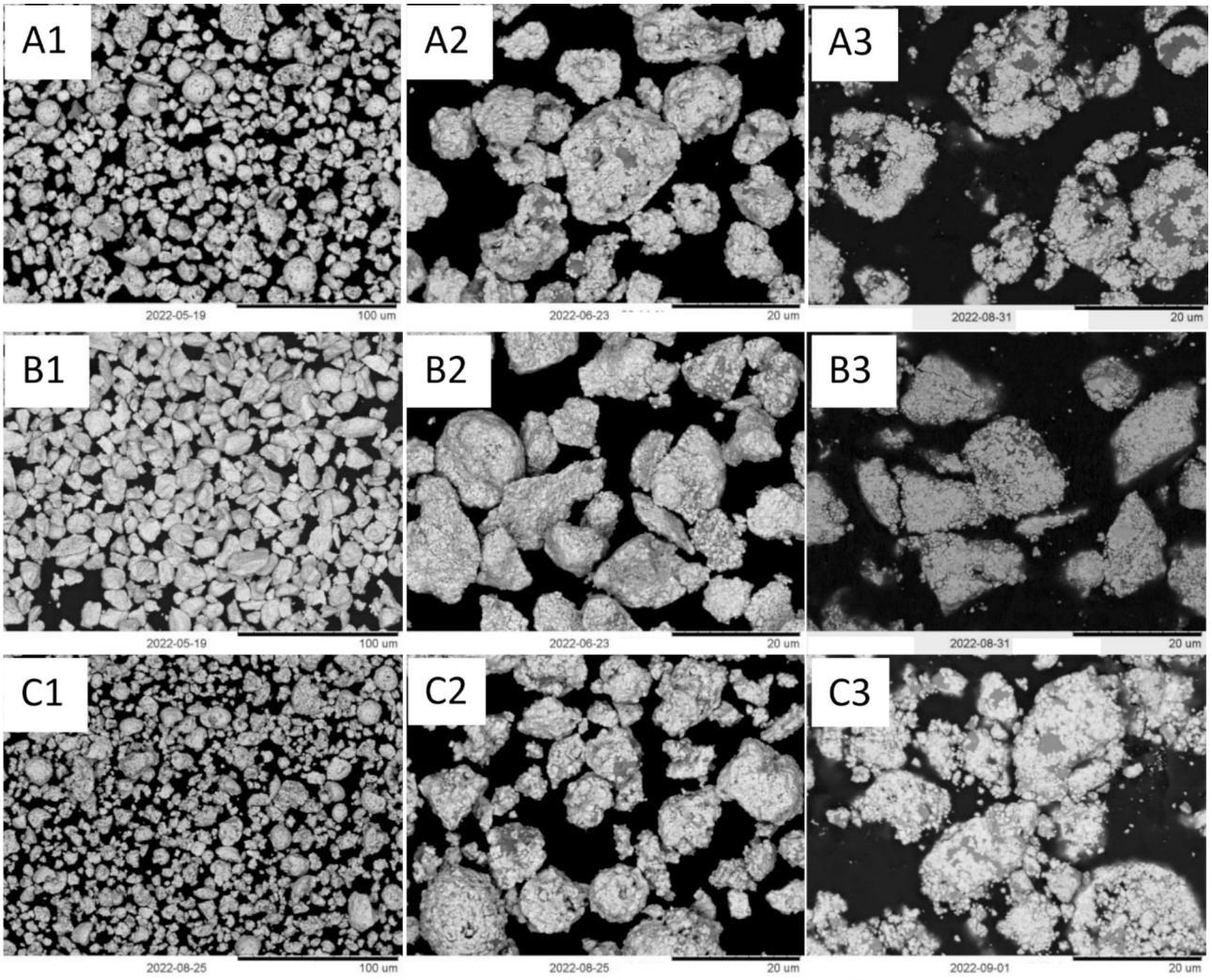

Fig. 2. SEM micrographs of the surface of the feedstock powders at low (x1000, A1, B1, C1) and high (x4000, A2, B2, C2) magnification, and corresponding cross-sectional views (x4000, A3, B3, C3): P1 (A1, A2, A3), P2 (B1, B2, B3), and P3 (C1, C2, C3) powders.

In post-wear analysis, the wear tracks on the coatings were observed by SEM (Quanta 200 and Nova NanoSEM-450, FEI Thermo Fisher Scientific, Eindhoven, NL), and EDS analysis (respectively: INCA, Oxford Instruments Analytical, Abingdon, UK; and Quantax200, Bruker) was employed for elemental distribution analysis.

2.5. Jet erosion testing

Dry jet erosion testing (using the AIR JET EROSION TR-470 test rig, DUCOM, India) was carried out according to the ASTM G76–07 standard [3] on polished samples with Ra < 0.2 μm, prepared following the same procedure described in Section 2.4. The samples were fixed during the test and were exposed to a jet of alumina particles with an average size of 50 μm. The parameters are summarized in Table 5. Three test repetitions were conducted for each sample with 60° and 90° impingement angles and two times for each sample with 30° impingement angle. The tests with a 60° impingement angle were not conducted on 50 μm-thick coatings. Samples were ultrasonically cleaned before and after each test.

Dry erosion tests performed on thinner coatings, specifically the P3N1–50 configuration, showed that, using the same parameters as the tests on thicker coatings, the erodent particles reached the substrate. Therefore, the test duration was reduced to 2:00, 1:30, and 1:00 until no visible traces of the substrate were detected. Therefore, the test durations were of 3:00 min for the 150 μm-thick coatings and 1:00 min for the 50 μm-thick ones.

Mass loss was measured by weighing the samples before and after the test using a laboratory weighing scale (PCE Deutschland GmbH) with a resolution of ±0.1 mg. Then, the volume loss was calculated by assuming 13.93 g/cm^3 as the density of WC-10Co4Cr.

3. Results and discussions

3.1. Powder characterization

Particle size distribution analysis (Fig. 1) revealed that all three powders possessed sizes suitable for HVAF deposition. P1, with a nominal particle size of 5–20 μm, exhibited a measured particle size range of 7 / 12 / 21 μm (d10 / d50 / d90). P2 and P3, whose nominal sizes were both in the range of 5–15 μm, exhibited distributions of 8 / 13 / 20 μm and 6 / 11 / 19 μm, respectively. Therefore, all feedstock powders exhibited very similar size distributions, characterized by a rather narrow range and a fine average size when compared to typical HVOF-grade thermal spray powders, which can be regarded as being well suited to a HVAF process especially for deposition of the thinner 50 μm thick coatings that were also targeted in the present study.

Examining the morphology, P1 demonstrated a nearly spherical shape indicative of its agglomeration and sintering manufacturing route (Fig. 2) [4]. However, micrographs revealed internal porosity and

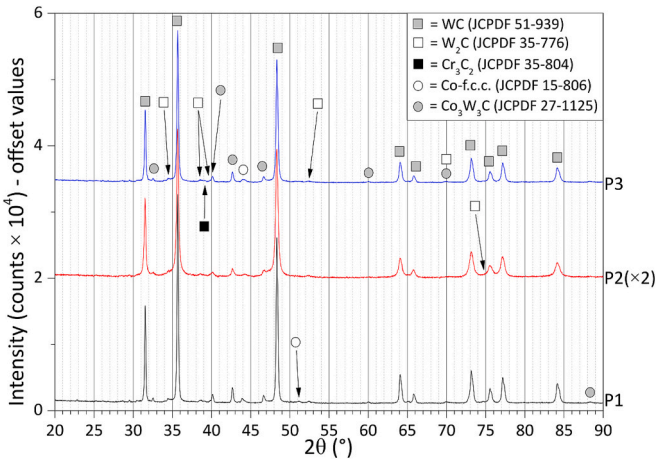

Fig. 3. XRD patterns of all feedstock powders used in this study.

binder accumulation areas within the particles. In contrast, P2, produced by sintering and crushing, displayed angular and blocky morphology with predominantly dense particles (Fig. 2 B). Micrographs showed minimal porosity and binder accumulation, suggesting a more homogenous microstructure compared to P1. Thus, the characteristics of the present feedstock materials conform to the typical features of powders obtained by the two respective manufacturing processes as described in the.

Introduction. The P3 powder exhibited intermediate features between the former two, as expected (Section 2.1): particles are irregularly shaped but some possess nearly spherical shapes (Fig. 2 C). Internal porosity and binder clusters were also observed, though to a lesser extent compared to P1.

Chemical analysis via energy-dispersive X-ray spectroscopy (EDS) confirmed the presence of tungsten carbides and metallic binder in all three powders. The X-ray diffraction (XRD) analyses of the powders are almost identical from the point of view of the phase constitution (Fig. 3): WC is the primary phase in each powder, with minor amounts of Co-f.c.c. and of the secondary carbide phases W_2C and Co_3W_3C. Many studies

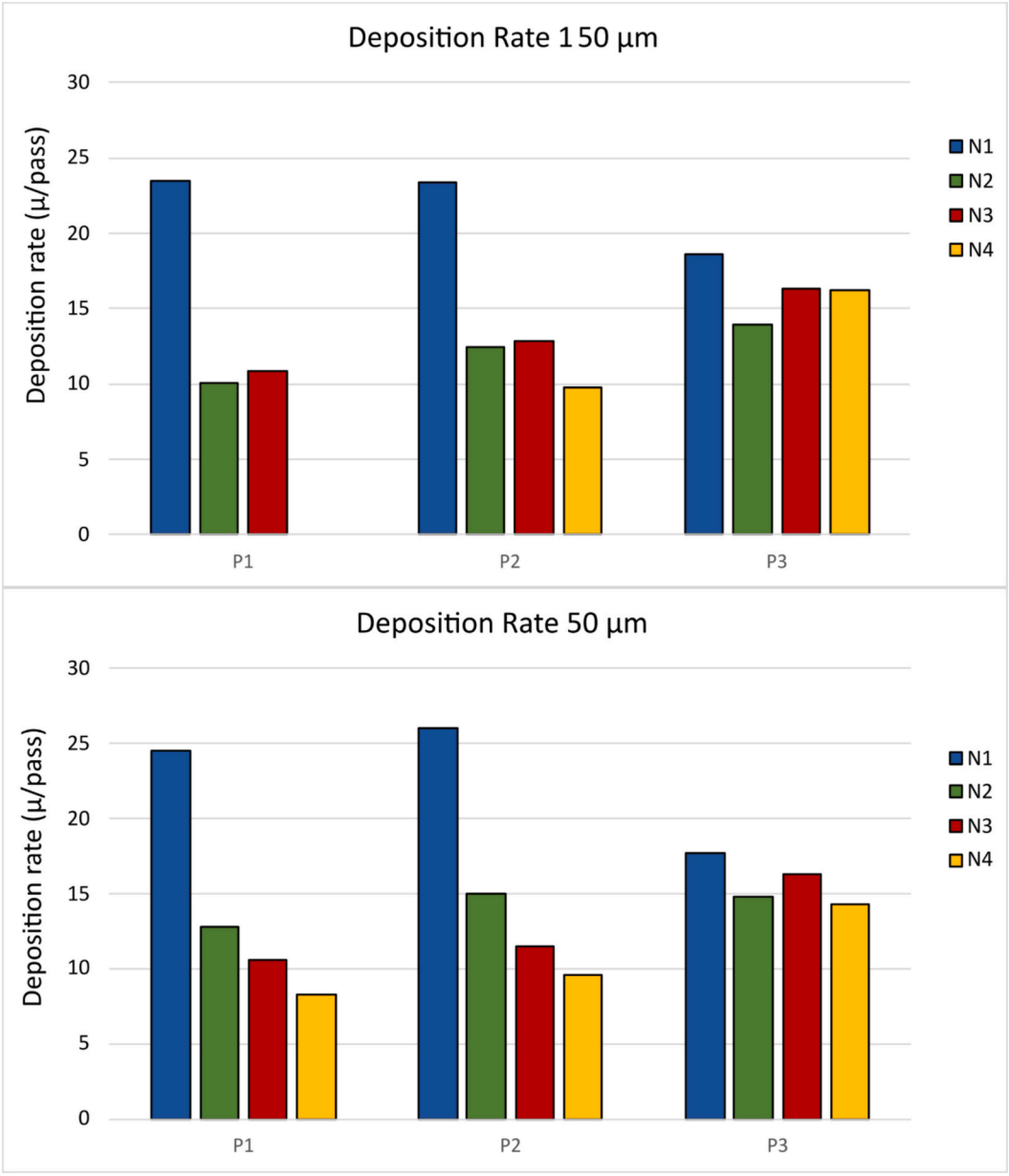

Fig. 4. Deposition rate for P1, P2, P3 powders sprayed using four different nozzles.

Table 6
Average roughness (Ra) for all the coatings.

	P1		P2		P3	
Coating thickness [μm]	50	150	50	150	50	150
N1	2.19 ± 0.14 μm	2.39 ± 0.14 μm	2.13 ± 0.20 μm	2.30 ± 0.07 μm	2.30 ± 0.30 μm	2.30 ± 0.14 μm
N2	1.81 ± 0.03 μm	2.15 ± 0.21 μm	1.76 ± 0.07 μm	1.87 ± 0.14 μm	1.63 ± 0.08 μm	1.93 ± 0.05 μm
N3	2.03 ± 0.15 μm	2.40 ± 0.50 μm	1.56 ± 0.07 μm	1.69 ± 0.05 μm	1.57 ± 0.12 μm	1.67 ± 0.06 μm
N4	1.74 ± 0.08 μm	-	1.89 ± 0.36 μm	1.62 ± 0.07 μm	1.74 ± 0.19 μm	1.97 ± 0.15 μm

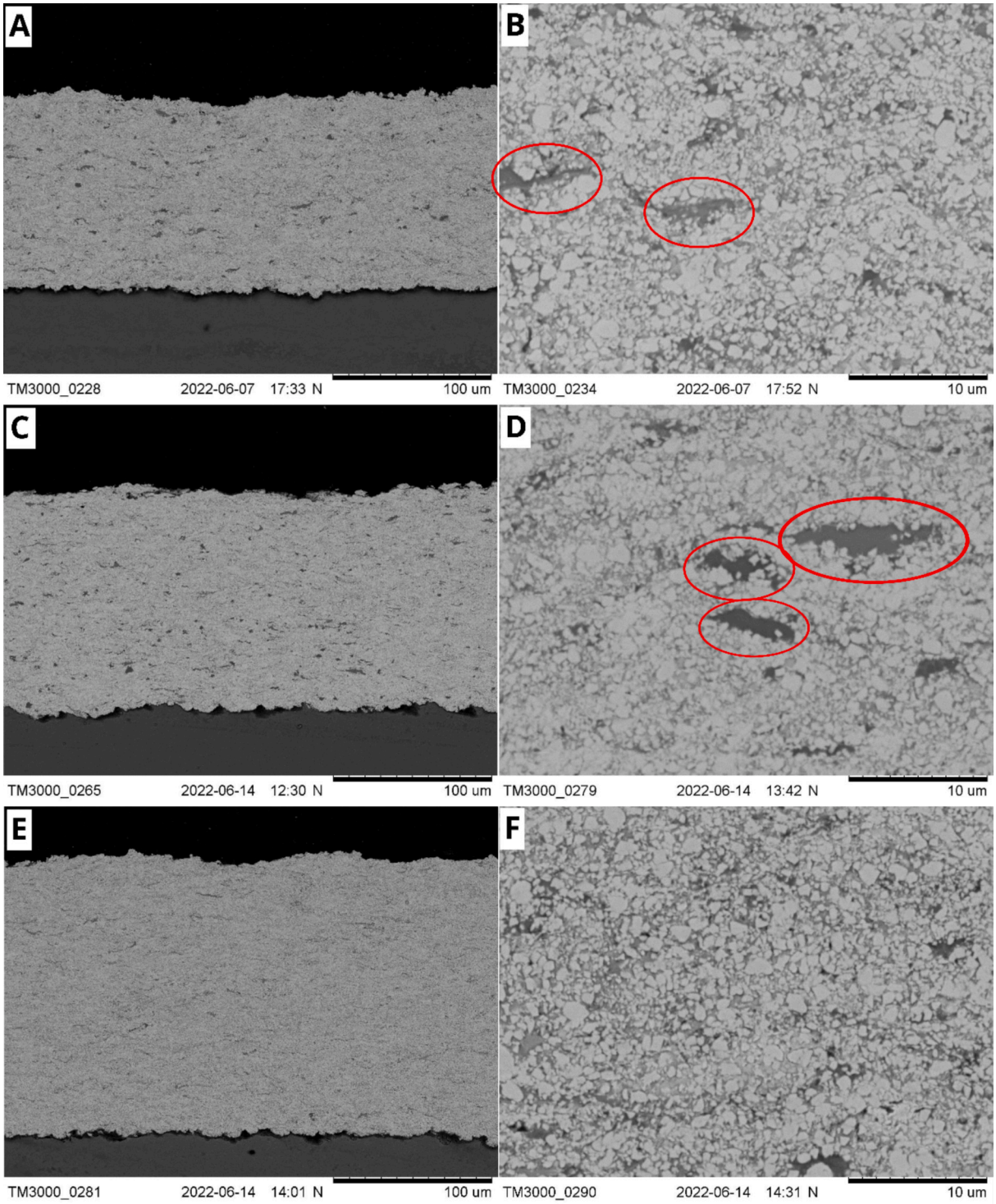

Fig. 5. SEM micrographs of the cross-sections of the 150 μm-thick coatings obtained from the P1 powder: N1(A, B), N2 (C, D), N3 (E, F).

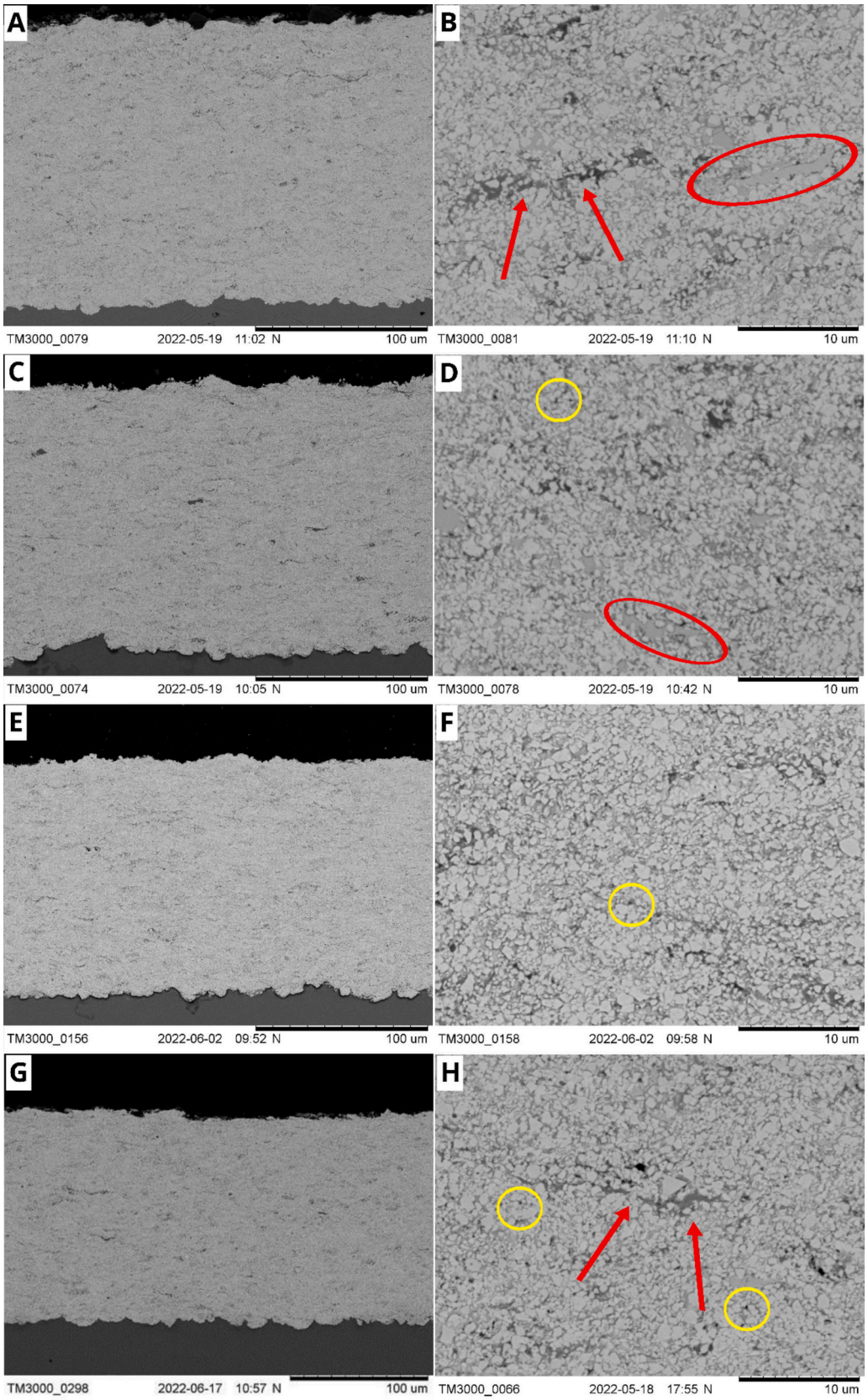

Fig. 6. SEM micrographs of the cross-sections of the 150 μm-thick coatings obtained from the P2 powder: N1(A, B), N2 (C, D), N3 (E, F), N4 (G, H).

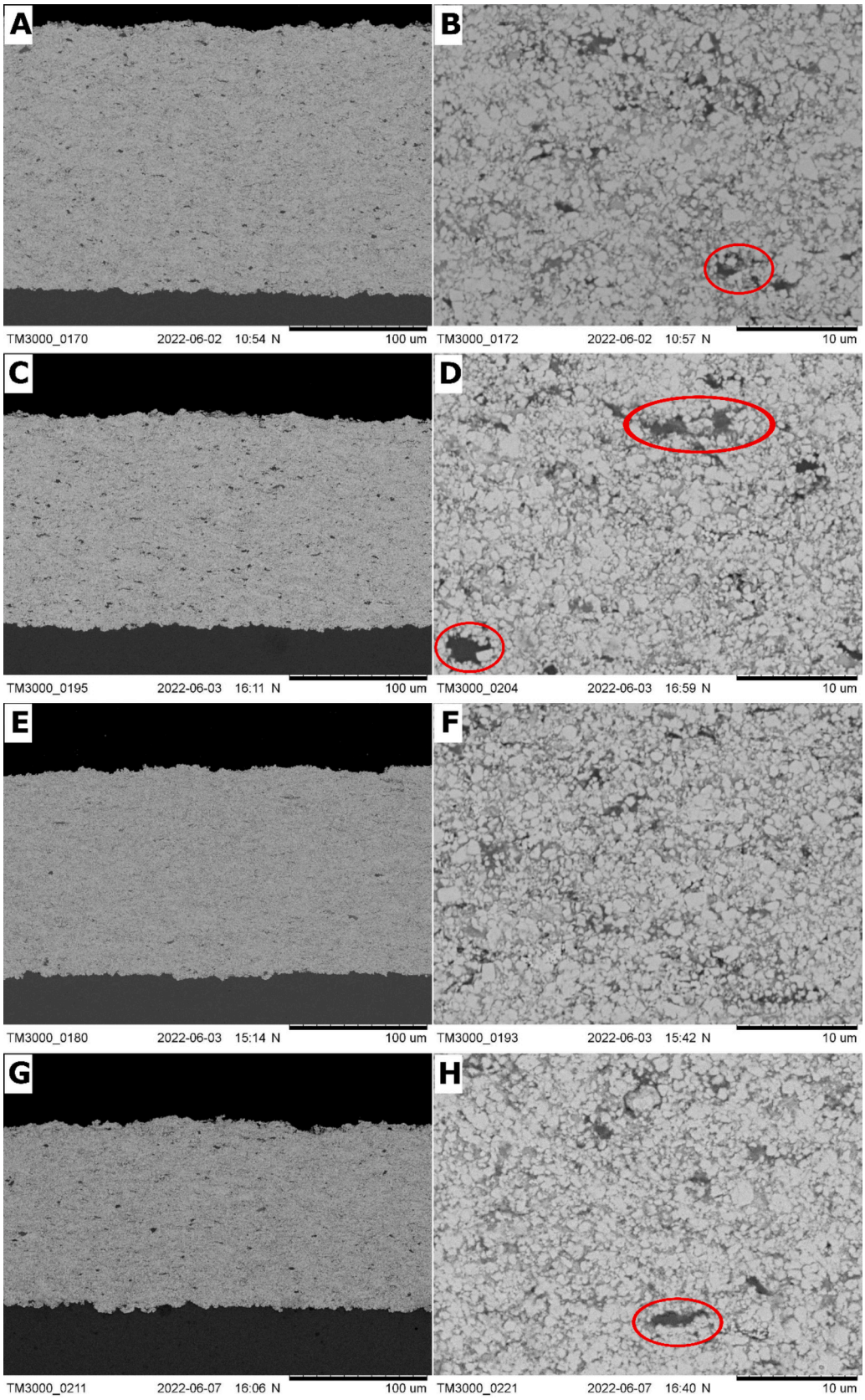

Fig. 7. SEM micrographs of the cross-sections of the 150 μm-thick coatings obtained from the P3 powder: N1(A, B), N2 (C, D), N3 (E, F), N4 (G, H).

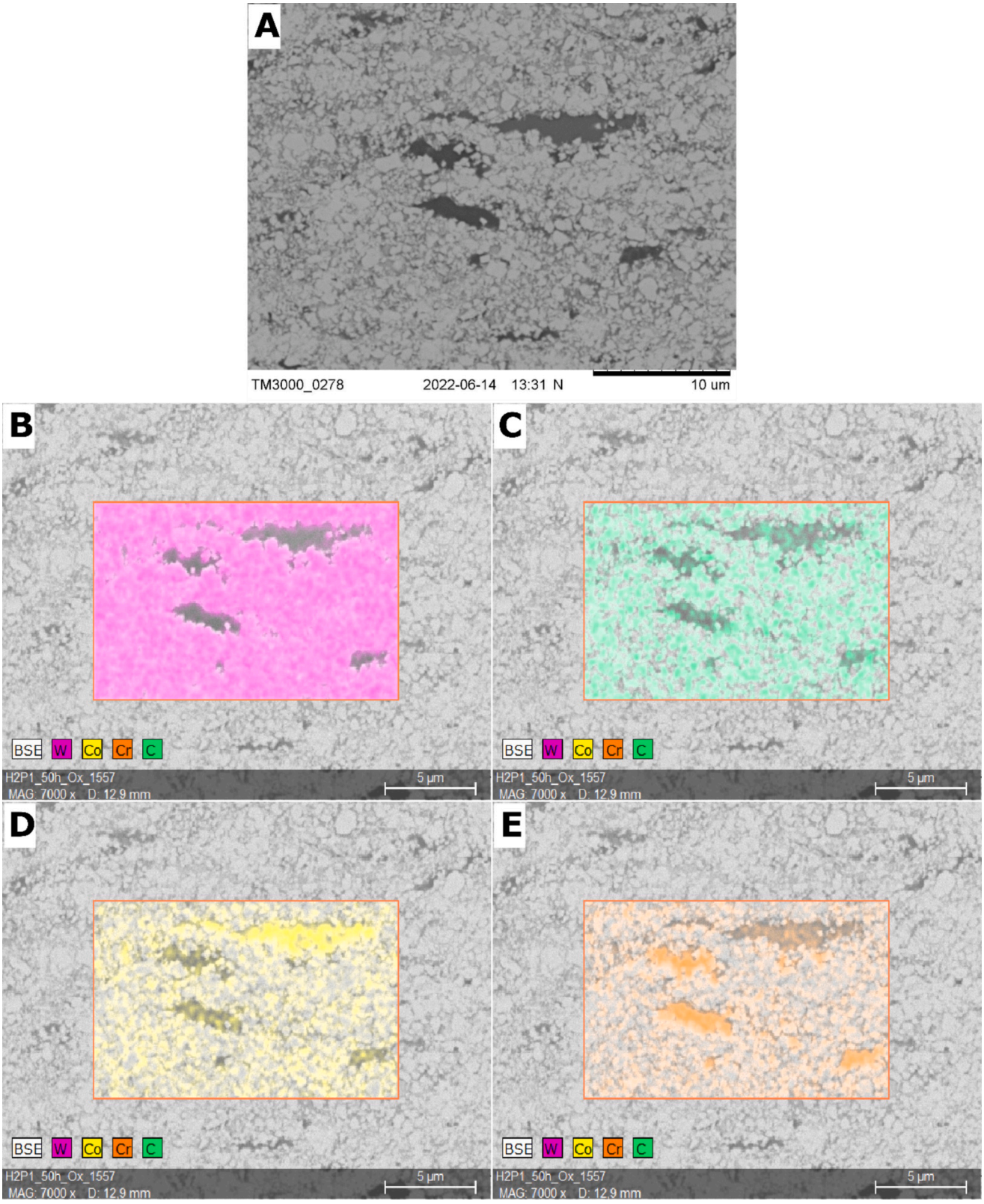

Fig. 8. EDS elemental mapping on the cross-section of the P1N2 coating: A) SEM micrograph, and maps of B) W, C) C, D) Co, E) Cr.

have detected these secondary carbides that most likely develop during sintering in this kind of powders [15,16,22]. P2 and P3 exhibited slightly broader peaks compared to P1, possibly because the initial sintering of the bulk pellets in the S&C process was carried out at sufficiently high temperatures and/or for sufficiently long times to result in an increase in crystal size and healing of lattice defects.

3.2. Deposition process

Each powder was deposited with various nozzle configurations,

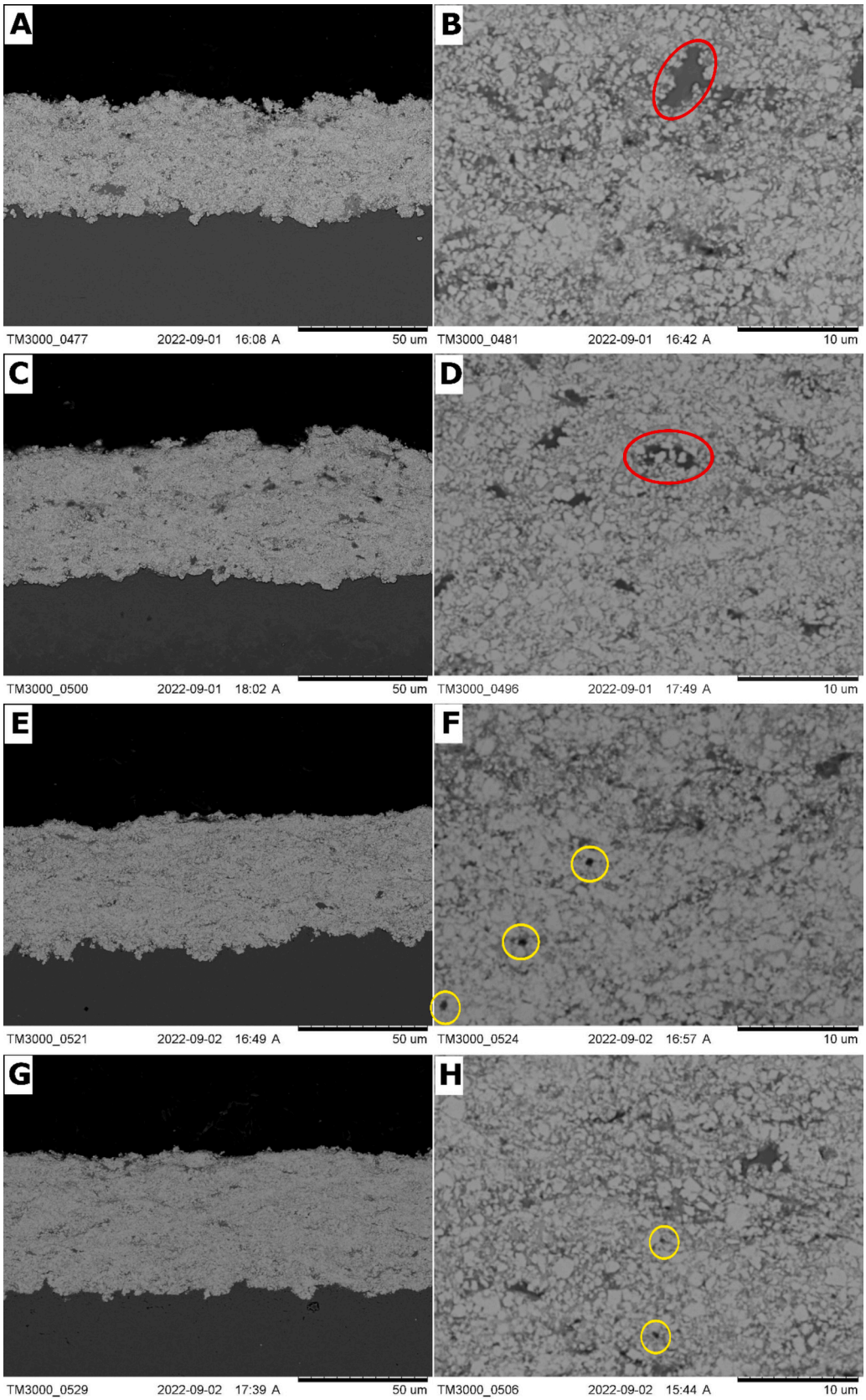

Fig. 9. SEM micrographs of the cross-sections of the 50 μm-thick coatings obtained from the P1 powder: N1(A, B), N2 (C, D), N3 (E, F), N4 (G, H).

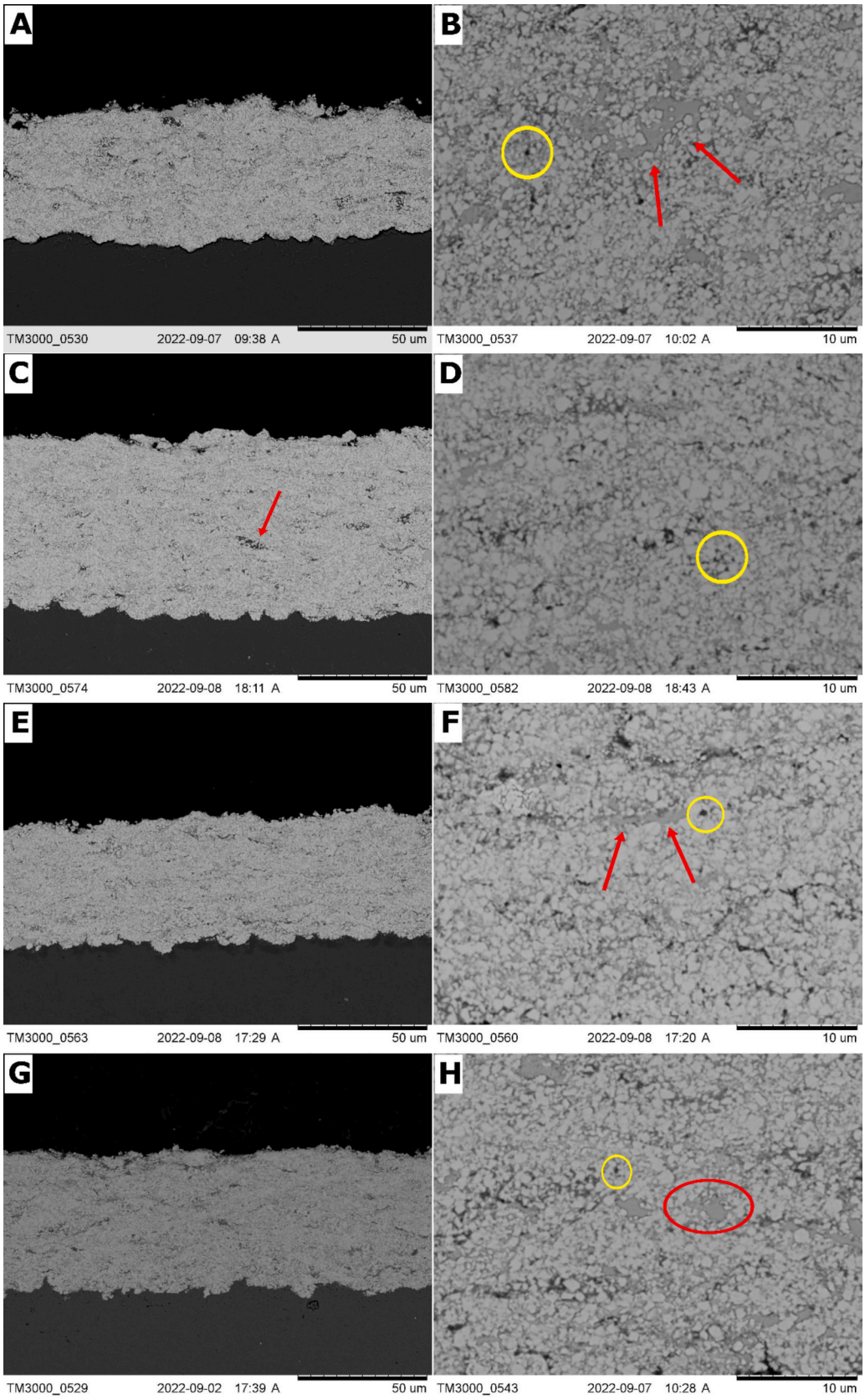

Fig. 10. SEM micrographs of the cross-sections of the 50 μm-thick coatings obtained from the P2 powder: N1(A, B), N2 (C, D), N3 (E, F), N4 (G, H).

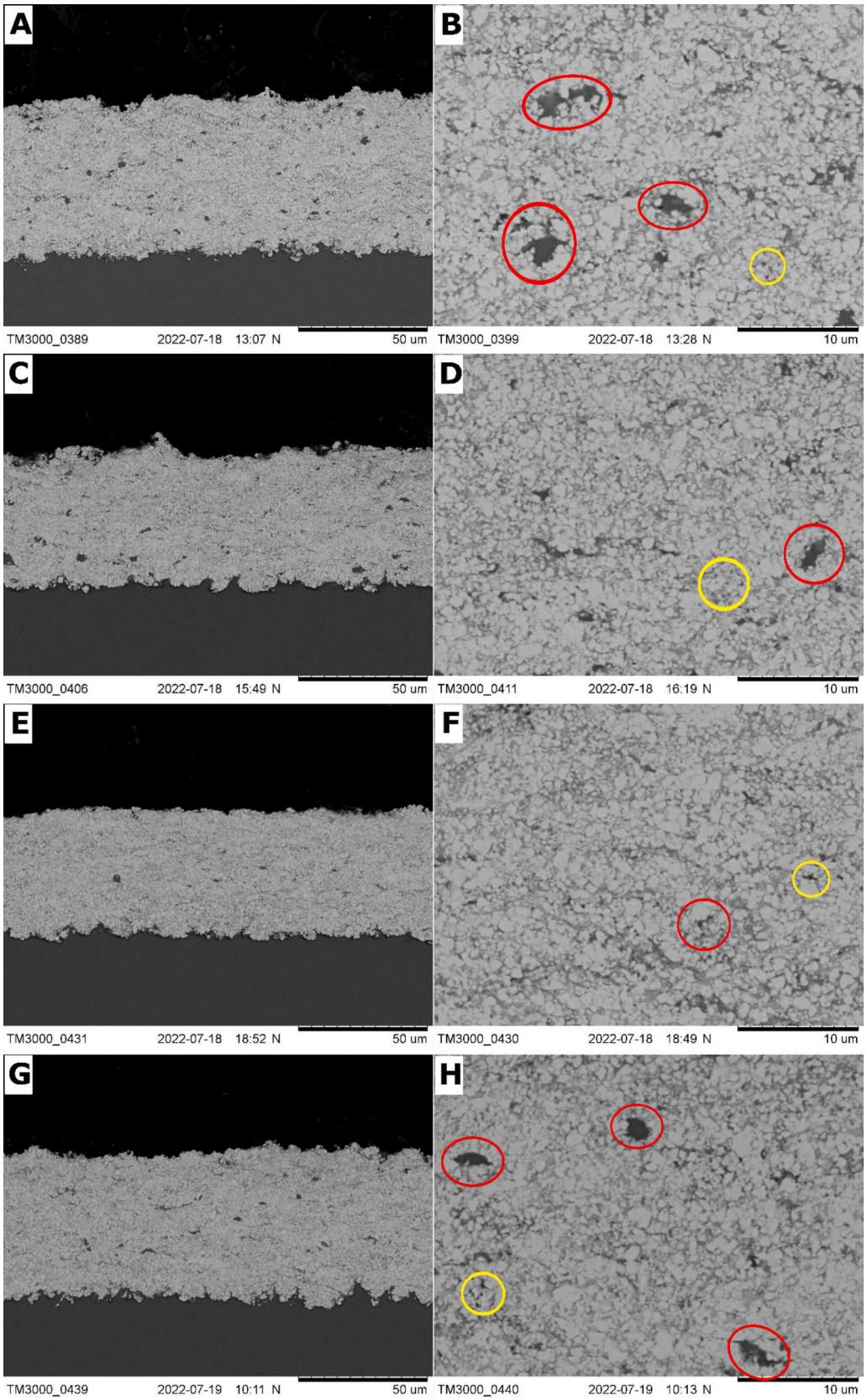

Fig. 11. SEM micrographs of the cross-sections of the 50 μm-thick coatings obtained from the P3 powder: N1(A, B), N2 (C, D), N3 (E, F), N4 (G, H).

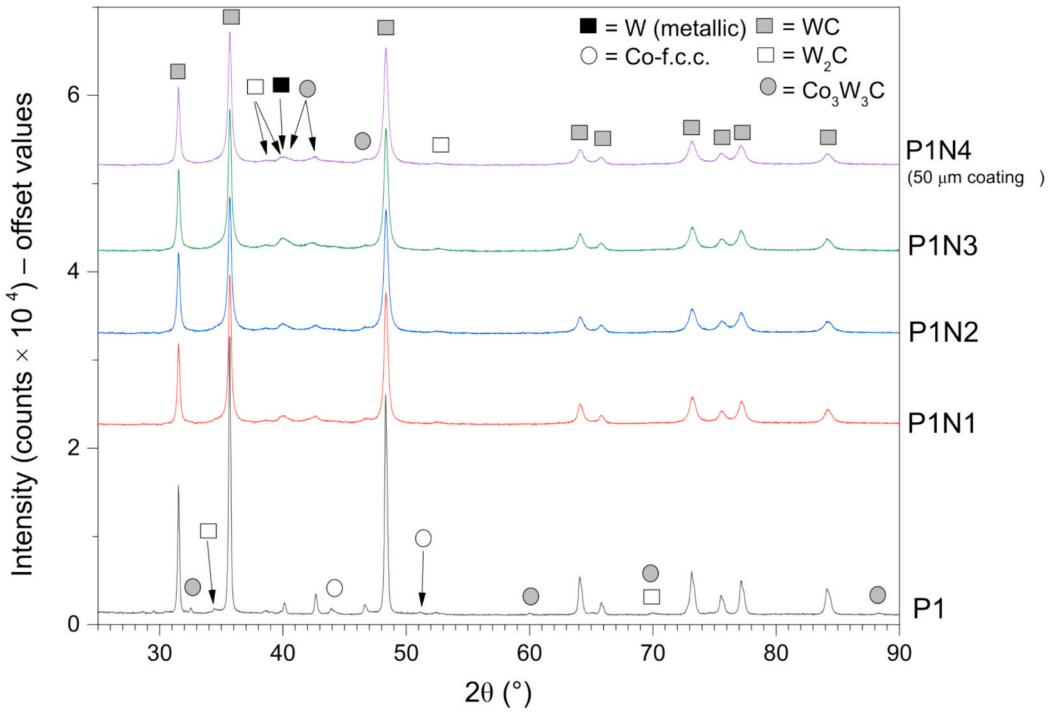

Fig. 12. XRD patterns of the P1 feedstock powder and of all corresponding 150 μm WC–CoCr coatings (except for P1N4).

offering distinct outcomes. Average thicknesses of 50 μm and 150 μm were achieved with a maximum deviation from the target thickness of 15 %. Fig. 4 presents deposition rates for coatings produced using different nozzle configurations. Notably, the N1 configuration consistently displayed higher deposition rates across all powders. This trend can be attributed to the nozzle's characteristics, such as dwell time and exit diameter, affecting particle velocity; the significant difference in deposition rates between the N1 and N2 configurations suggests that the deposition rate of the M2 gun spraying process is significantly affected by the exit diameter of the nozzle as a larger nozzle exit diameter is known to expand the gases to higher velocity and lower temperature [23,24]. The correspondingly faster, colder particles have a greater likelihood to rebound upon impact.

The P1 and P2 powders exhibited similar trends in deposition rates among different configurations, with only marginally higher deposition rates for the P2 powder under most of the deposition conditions. This result can be analyzed from various perspectives. Factors such as powder porosity [25], carbide particle size [26,27], and substrate hardness and roughness [28] can impact the ability of powder particles to flatten upon impact on the substrate and, thus, influence deposition efficiency. Successful bonding necessitates intimate conformal contact surfaces resulting from particle flattening, which can enhance deposition efficiency. Porous particles usually exhibit better deformation or flattening ability upon impact compared to dense particles, resulting in a lower chance of rebounding [25].

The P3 powder exhibited a more uniform behavior, its deposition rate being much less dependent on the deposition conditions. Its deposition efficiency is higher especially with N2, N3, and N4 configurations. Considering that the particle porosity level and particle morphology are the only changed parameters among the powders, the results suggest that the P3 powder might have reached a suitable compromise in terms of shape and density of the particles, leading to improved deposition efficiency.

The average roughness (Table 6) of all the coatings was found to be comparable. Despite the higher number of passes, the roughness values for the 150 μm-thick coatings are comparable to those for the 50 μm coatings. The promisingly low roughness confirms the potential of the HVAF technique for industrial applications, which can reduce post-processing costs. Additionally, also in consideration of the lower number of passes, the average roughness of the coatings deposited with the N1 configuration, for both the 150 μm and 50 μm thickness, is higher compared to the other configurations. This also looks consistent with the expected lower particle velocity at impact for this nozzle configuration, resulting in less flattening and, therefore, higher roughness.

3.3. Coating microstructure

The microstructural analysis of WC-based coatings derived from P1, P2 and P3 powders reveals insights into their uniformity, porosity, and phase composition. Despite variations in deposition parameters, the coatings exhibit comparable characteristics, such as crack-free interfaces and low porosity content (<1 %).

Fig. 5, Fig. 6 and Fig. 7 illustrate the cross-sections of the 150 μm-thick coatings obtained from the P1, P2 and P3 powders, respectively. They highlight dense and uniform microstructures with carbide particles ranging from 0.1 to 1 μm in all cases. Notably, binder-rich areas, indicated by circles in the high-magnification micrograph, are detectable especially in the coatings obtained from the P1 (Fig. 5) and P3 (Fig. 7) powders, and particularly in those deposited with the M2 gun configurations (panels B, D in Fig. 5 and Fig. 7). This means that the microstructural features of the corresponding feedstock materials, which indeed contained more matrix "lakes" than the P2 one, were carried over to the coatings, in particular when no secondary fuel injection was involved. In addition, all coatings retain even the smallest carbide particles. HVAF deposition achieves this by heating particles only up to (but not above) the melting point of the matrix, ensuring that microstructural changes and thermal alterations (e.g. dissolution and decarburization of WC) of the feedstock materials are minimized, whilst particle flattening and densification are simultaneously enhanced by their high impact velocity [23,29]. Under the M2 configuration, the temperature of the particles is even lower due to the lack of secondary combustion in the expansion nozzle. In contrast, the HVOF technology does not fully follow this trend due to the higher process temperatures, resulting in the dissolution and decarburization of some of the carbide particles. This

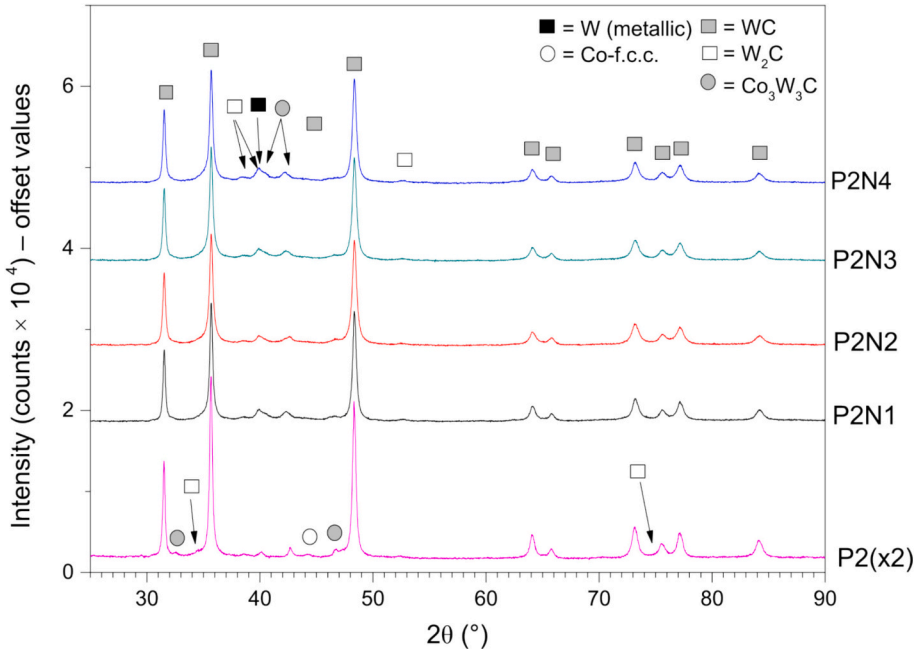

Fig. 13. XRD patterns of the P2 feedstock powder and of all corresponding 150 μm WC–CoCr coatings.

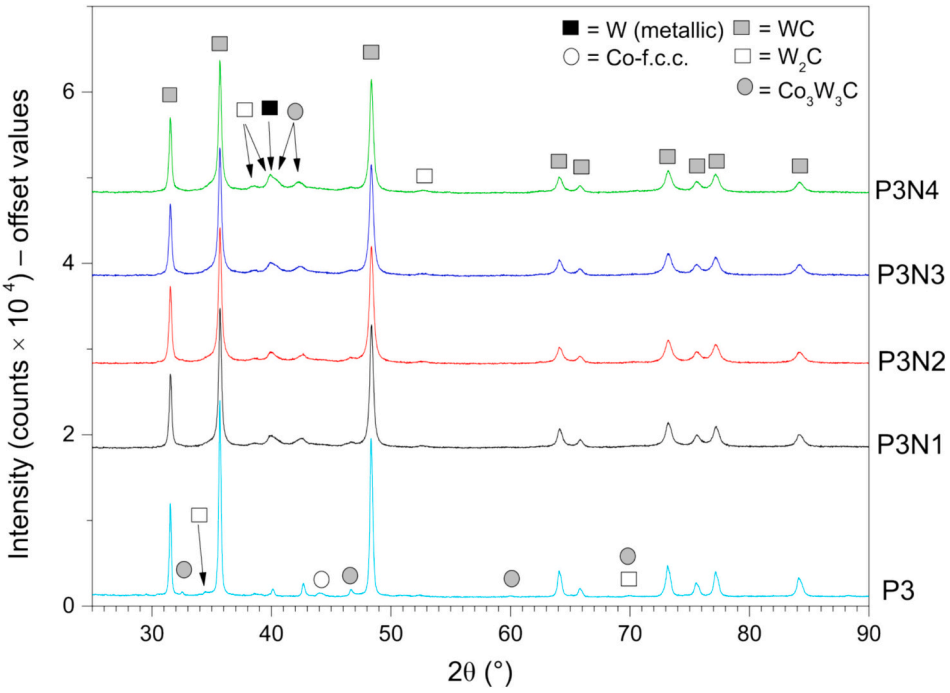

Fig. 14. XRD patterns of the P3 feedstock powder and of all corresponding 150 μm WC–CoCr coatings.

demonstrates how the HVAF method offers sufficient thermal and kinetic energy to flatten particles and create a dense structure without introducing unwanted thermal alterations to the injected powder feedstock. The precise physical mechanisms underlying the coating build-up process are still subject to debate [30].

EDS mapping (Fig. 8) reveals that two distinct types of matrix "lakes" exist: the dark gray regions correspond to Cr-rich phases, while the light gray regions correspond to Co-rich phases. However, certain regions of the WC-CoCr coating's matrix exhibit an even lighter contrast and a higher amount of W, suggesting that some WC may have slightly dissolved in the matrix even during the HVAF spraying process.

Comparatively, Fig. 9, Fig. 10 and Fig. 11 show the microstructure of the 50 μm-thick coatings, exhibiting similar characteristics to the 150 μm-thick coatings but with a slightly higher amount of small pores (indicated by yellow circles in the high-magnification micrograph), attributed to reduced shot-peening effects due to the fewer deposition passes. The micrographs once again demonstrate some retention of binder-rich regions, similar to the 150 μm coatings (indicated by red arrows and circles), particularly in the coatings obtained from the P1 and P3 feedstock and using the M2 configuration (Fig. 9B, D; Fig. 11B, D).

XRD analyses in Fig. 12, Fig. 13 and Fig. 14 confirm that

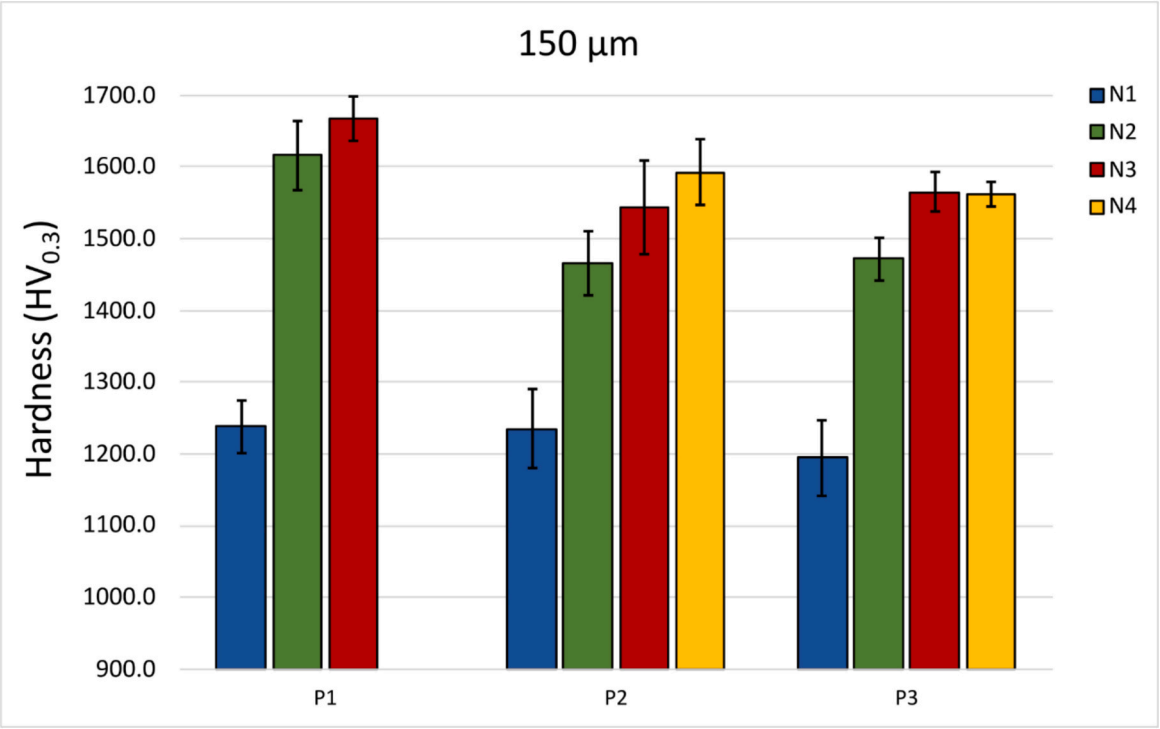

Fig. 15. Microhardness values for all 150 µm coatings.

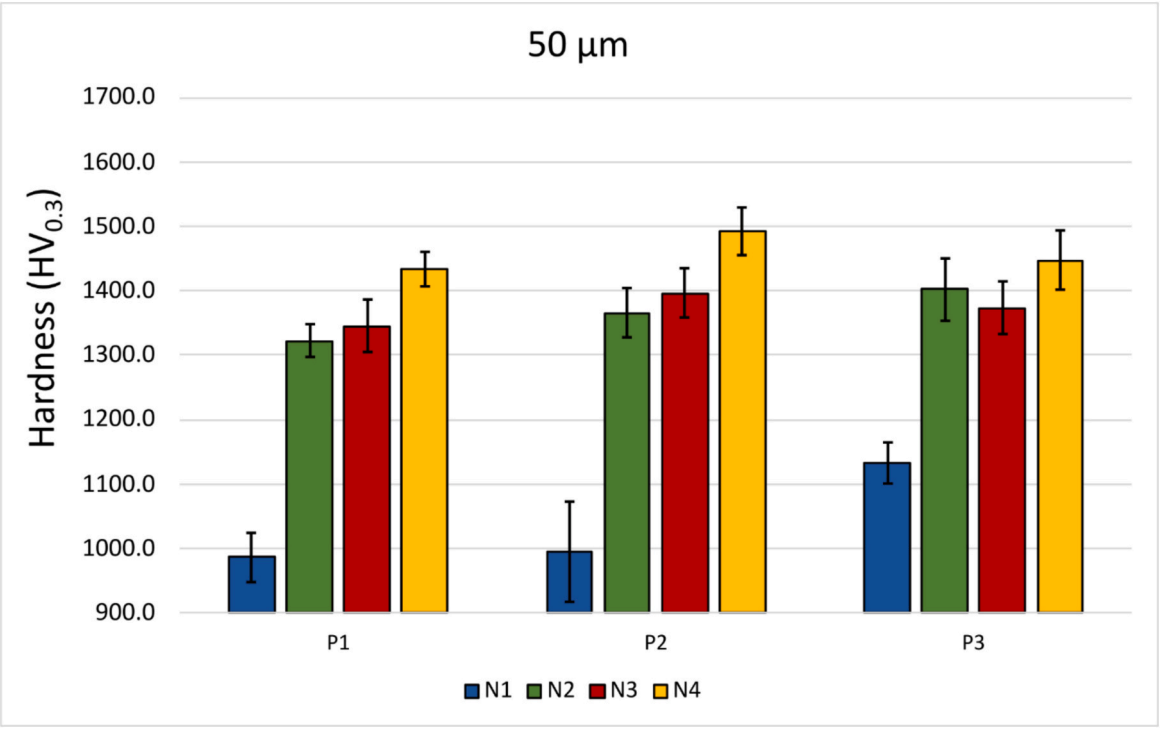

Fig. 16. Microhardness values for all 50 µm coatings.

decarburization, though present, is minimal. This is consistent with other research on the HVAF technique [14]. The literature reports conflicting results regarding the effect of the degree of decarburization/dissolution of W_2C on mechanical properties (e.g., favorable [31] or unfavorable [17]), though it should be noted that these studies employed the HVOF process. As shown by Verdon et al. [32], the HVOF process must find a compromise between heating the particles enough to obtain good flattening at impact, and not heating them too much to cause any significant decarburization. Thus, depending on the specific conditions employed in an HVOF study, an increased decarburization might be associated with improved flattening at impact and better cohesion, or excessive embrittlement. In the HVAF process, on the other hand, the higher particle impact velocity and lower process temperature ensure that decarburization can be kept low whilst achieving proper

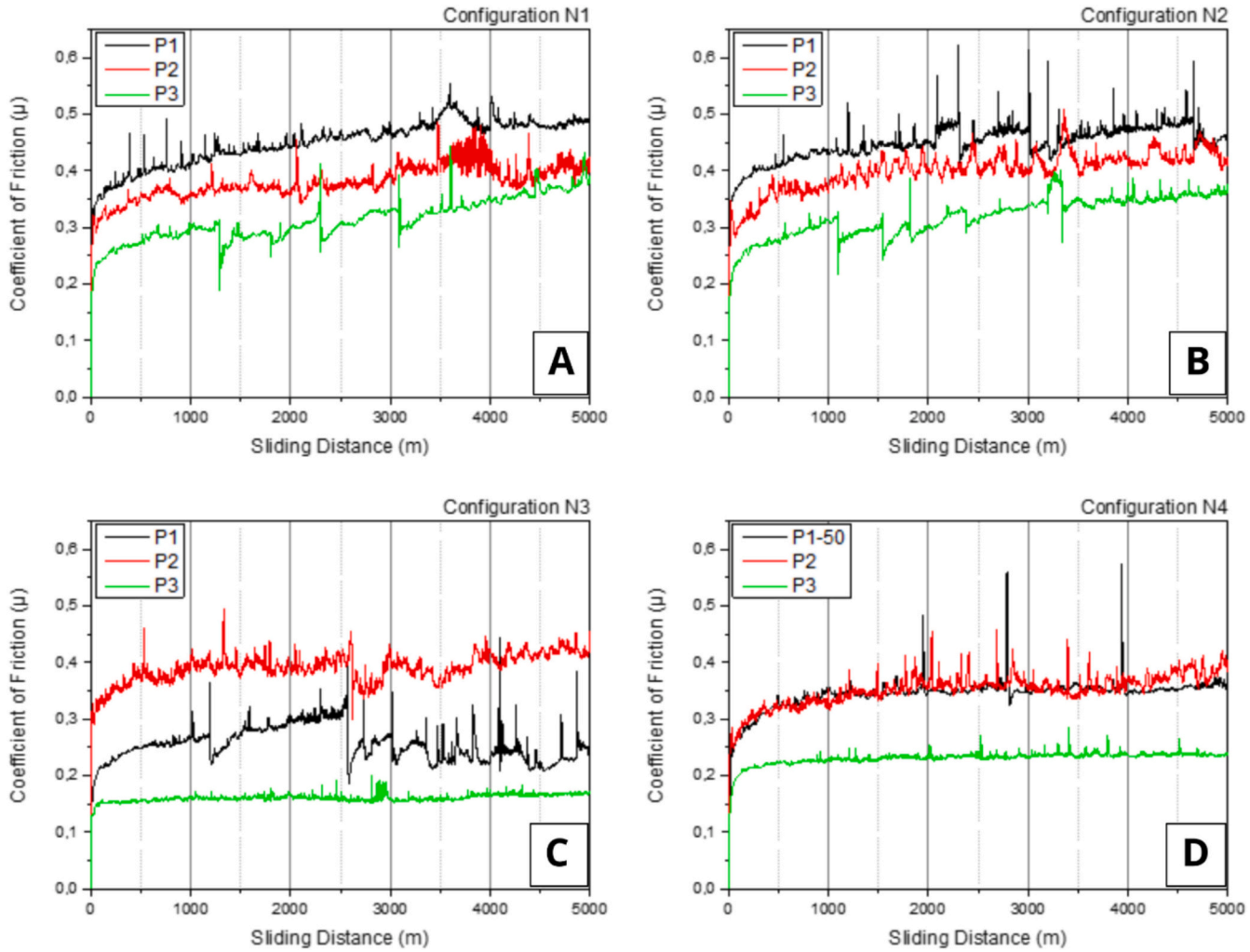

Fig. 17. Typical evolution of CoF for the 150 μm-thick coatings with different nozzle configurations: A) N1, B) N2, C) N3, D) N4.

flattening and strong cohesion. The broader diffraction peaks observed in the patterns of the coatings compared to those of the powder may be attributed to the significant plastic deformation of particles upon impact, making it more challenging to distinguish the Co-f.c.c. phase peaks in the former [29].

3.4. Microhardness test

The microhardness analysis of coatings derived from P1, P2 and P3 powders reveals variations influenced by deposition parameters and powder characteristics. Fig. 15 and Fig. 16 present the microhardness values of coatings with a thickness of 150 μm and 50 μm, respectively. Two major influential factors can be identified. The first is the coating thickness: the 50 μm samples have systematically lower hardness than 150 μm-thick coatings. The lower average hardness value observed in the thin coatings could be attributed, on the one hand, to the reduced peening effects on coatings deposited with a lower number of passes. On the other hand [33], in the case of the 50 μm samples, the indentations were performed in the middle of the cross-sections, with average diagonals of approximately 23 μm, leaving only about 15 μm of distance from the interfaces. This contrasts with the 150 μm samples, where the coating thickness was sufficient to maintain a suitable distance between the indents and the interfaces. Thus, the lower hardness of the 50 μm samples could be partly an artefact due to the proximity of the indents to the interface with the softer substrate and the mounting material [33].

The other most influential factor are the deposition conditions. In almost all cases, the coatings deposited under the M2 conditions (N1 and N2) are less hard than those deposited under the M3 conditions (N3 and N4), which produce simultaneously higher particle velocity and temperature at impact. In particular, the N1 conditions, characterized by a small nozzle exit diameter that results in less expansion and acceleration of the gas and the particles, results in coatings that have far lower hardness than the others. The N4 conditions, with a larger exit diameter to provide improved expansion and acceleration and a secondary air-fuel combustion in the expansion nozzle itself, usually results in the hardest coatings since very high impact velocities are coupled with adequate particle temperatures [23]. High impact velocities result in stronger cohesion and more pronounced peening effects, both of which contribute to increased hardness. [34]

3.5. Dry sliding wear resistance

Fig. 17 and Fig. 18 show the typical evolutions of the coefficient of friction (CoF) during the ball-on-disk sliding wear tests performed on the 150 μm-thick and 50 μm-thick coatings, respectively. The CoF increases more rapidly during the initial 1000 m, and then tends to a steady state. However, notable differences emerge especially as a function of the feedstock powder type and, secondarily, the process conditions. The coatings obtained using the P3 powder usually produce lower and more stable CoF values at the steady state, especially when deposited using the M3-type torch configuration (N3 and N4 conditions). The coatings from the P1 and P2 powders, by contrast, exhibit higher friction

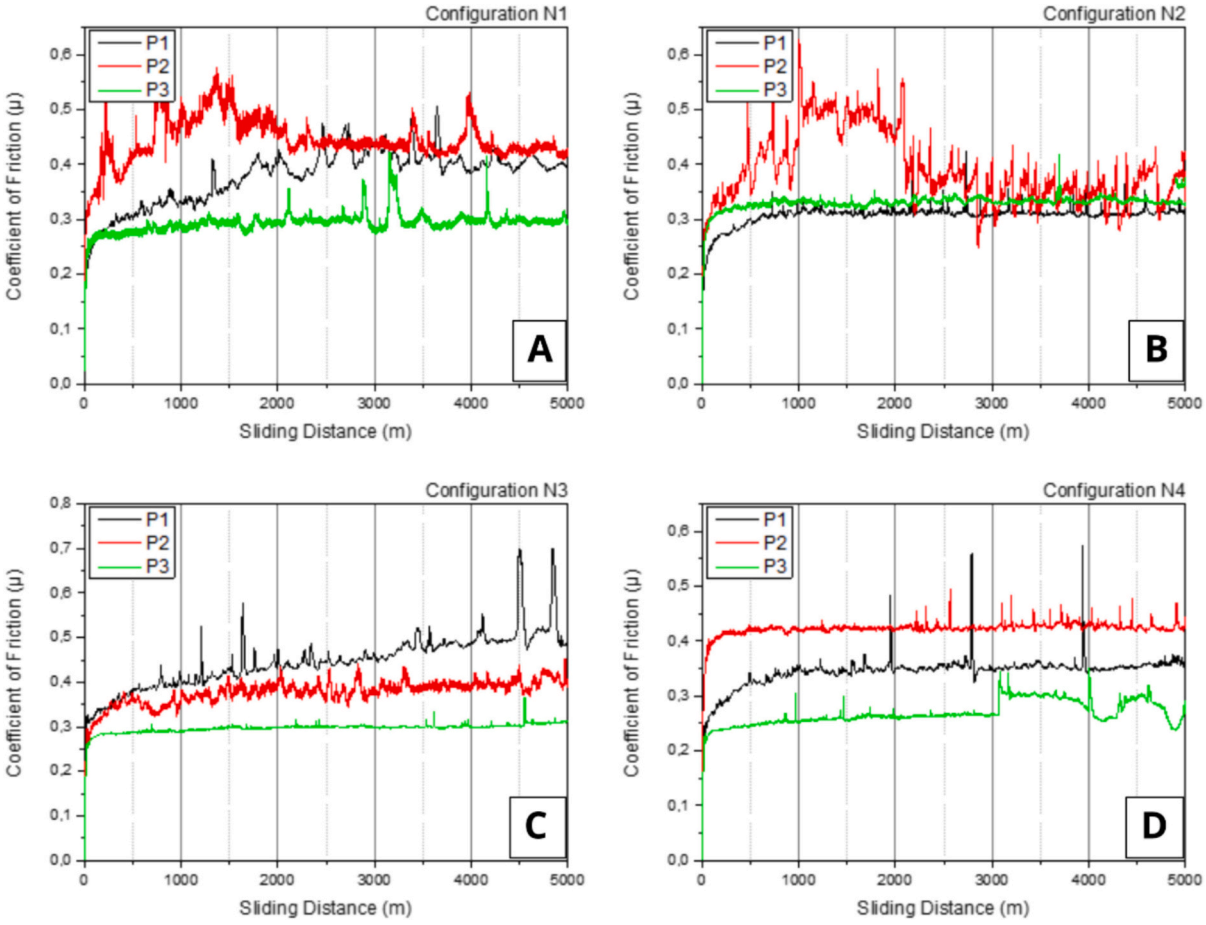

Fig. 18. Typical evolution of CoF for the 50 μm-thick coatings with different nozzle configurations: A) N1, B) N2, C) N3, D) N4.

Table 7
Average steady state CoF values and specific wear rates (WR) for the 150 μm-thick coatings, and corresponding standard deviations.

Powders	Nozzle configuration	Average CoF	Std. dev.	WR [mm^3/(N•m)]	Std. dev.
P1	**N1**	0.41	0.04	1.13×10^{-8}	0.24×10^{-8}
	N2	0.36	0.08	1.19×10^{-8}	0.11×10^{-8}
	N3	0.32	0.09	1.60×10^{-8}	0.31×10^{-8}
P2	**N1**	0.41	0.02	2.48×10^{-8}	0.23×10^{-8}
	N2	0.44	0.06	2.12×10^{-8}	0.36×10^{-8}
	N3	0.38	0.01	1.45×10^{-8}	0.14×10^{-8}
	N4	0.39	0.04	1.98×10^{-8}	0.13×10^{-8}
P3	**N1**	0.33	0.01	1.23×10^{-8}	0.64×10^{-8}
	N2	0.31	0.01	0.93×10^{-9}	0.23×10^{-8}
	N3	0.21	0.05	1.66×10^{-8}	0.36×10^{-8}
	N4	0.23	0.01	1.62×10^{-8}	0.48×10^{-8}

Table 8
Average steady state CoF values and specific wear rates (WR) for the 50 μm-thick coatings, and corresponding standard deviations.

Powders	Nozzle configuration	Average CoF	STD. DEV.	WR [mmˆ3/(N*m)]	STD.DEV.
P1	N1	0.40	0.07	2.62×10^{-8}	0.68×10^{-8}
	N2	0.31	0.01	3.41×10^{-8}	0.68×10^{-8}
	N3	0.38	0.05	3.03×10^{-8}	0.96×10^{-8}
	N4	0.37	0.04	3.28×10^{-8}	0.93×10^{-8}
P2	N1	0.36	0.09	4.72×10^{-8}	1.98×10^{-8}
	N2	0.48	0.10	3.26×10^{-8}	0.38×10^{-8}
	N3	0.40	0.03	3.96×10^{-8}	0.20×10^{-8}
	N4	0.35	0.07	2.54×10^{-8}	0.49×10^{-8}
P3	N1	0.32	0.08	2.79×10^{-8}	0.85×10^{-8}
	N2	0.30	0.03	2.26×10^{-8}	0.31×10^{-8}
	N3	0.38	0.07	2.83×10^{-8}	0.17×10^{-8}
	N4	0.32	0.04	2.36×10^{-8}	0.26×10^{-8}

coefficients with frequent, wide fluctuations even at the steady state. Sometimes, they retain a slightly upwards trend, without a full stabilization. Once again, even among the P1- and P2-series of samples, the N3 and N4 process conditions tend to result in fewer, narrower fluctuations than do the N1 and N2 ones, although the CoF values are always higher and far less stable than for the P3-series.

Table 7 and Table 8 present the average coefficient of friction (CoF) values at the steady state with the associated standard deviation determined based on the three test repetitions for each sample. These values confirm that the coatings derived from the P3 powder demonstrate lower CoF values compared to those obtained from the P1 and P2 powder in almost all cases, and more markedly among the 150 μm-thick samples, along with smaller standard deviation ranges in most cases. As noted previously, fluctuations in CoF values were also influenced by nozzle configurations: the N1 and N2 configurations resulted in coatings that produced higher friction coefficients than did the N3 and N4 configurations. This is true in all cases, but the difference is especially apparent with the coatings from the P3 powder. With the 50 μm-thick coatings, differences are a bit less clear, also because the associated standard deviations are often larger, even though the P3 powder still leads to lower average steady-state CoF values in most cases. On the other hand, the reduction in standard deviation is no longer perceivable, and there is no clear difference between the N1/N2 and the N3/N4 configurations. Perhaps, as substrate deformation becomes perceivable in these conditions, it blurs a bit the difference between the "intrinsic"

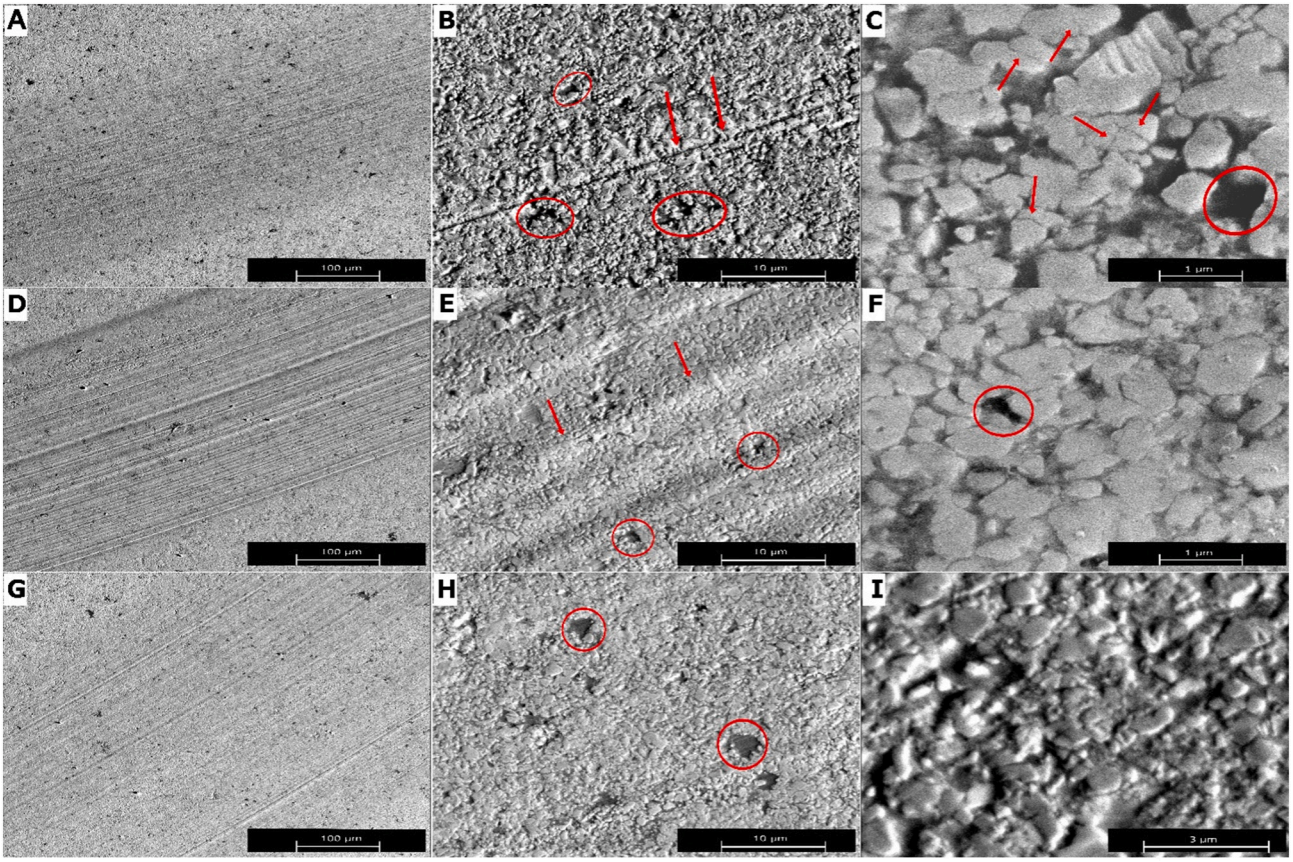

Fig. 19. SEM micrographs of the worn surfaces after ball-on-disk testing of the 150 µm-thick coatings deposited with the N1 configuration: P1 (A, B, C), P2 (D, E, F), P3 (G, H, I); arrows in panels B, E indicate shallow abrasive grooves; circles in panels B, C, E, F indicate pull-outs; arrows in panels C indicate carbide cracks.

response of the coating.

On the other hand, a clear correlation between specific wear rate and CoF value (Table 7 and Table 8) is not evident, indicating complex interactions between coating composition, deposition parameters, and wear behavior. The specific wear rates values listed in Table 7 and Table 8 are extremely low, of the order of 10^{-8} $mm^3/(N{\cdot}m)$, indicating a mild wear regime [34]. These results are consistent with previous studies, emphasizing the specific wear rates $<10^{-7}$ $mm^3/(N{\cdot}m)$ for HVAF WC-CoCr coatings [13,35]. Among the coatings with similar thickness, there is no clear trend of the specific wear rates as a function of the deposition conditions, and no clear correlation with the hardness values previously shown in Fig. 15 and Fig. 16. It should be noted that the specific wear rate values are associated with a quite high experimental error: the relative error on the data in Table 7 and Table 8 in in most cases between 10 % and 30 %, with a couple of values having an error as large as ~ 40 % or 50 %. Whilst it is known that wear loss data is usually associated with a large experimental scatter [36], it is possible that this scatter was at least in part contributed to having performed wear tests with different track radii, as explained in Section 2.4. This scatter might have, in turn, covered some weak correlations between specific wear rates and other parameters. In any case, among the 150 µm-thick coatings (Table 7), those deposited using the P1 and P3 powders seem to demonstrate slightly better wear resistance than those obtained from the P2 (S&C) powder, especially when comparing coatings sprayed with the M2 gun (N1 and N2).

The only, truly clear difference among the samples is that as a function of the thickness of the coating. The specific wear rates of the 50 µm-thick coatings (Table 8), which are in the range of 2 to 4 × 10^{-8} $mm^3/(N{\cdot}m)$, are approximately twice those of the 150 µm coatings (Table 7) in most cases. This means that, whilst all the coatings are sufficiently thick to withstand the stress distribution caused by the alumina contact during testing without macroscopic damage, cracks, or delaminations, the thickness does play a role. The wear performance of a coating can, indeed, be influenced by its thickness, particularly when applied to soft substrates. When in contact with a rigid ball counterpart, high Hertzian contact stresses are introduced to the coating/substrate system. The maximum Hertzian stress may occur within the coating or the substrate, depending on the coating thickness and the contact conditions [37]. Substrate deformation occurs when the coating thickness is low enough that a significant portion of the applied stress is borne by the substrate [38]. Deformation of the substrate results in a bit more stress being placed onto the thinner coating, which is forced to bend in response to such deformation. The peening effect and its impact on the coating's wear performance are also important factors to consider. In thicker coatings, the sub-layers experience a higher number of passes, meaning more hard particles impacting the surface and resulting in a more pronounced peening effect, as noted in Section 3.4. However, the depth of the present wear tracks was in most cases no >1 µm, and the grinding process mentioned in Section 2.4 had the sole purpose to remove the surface roughness, i.e., it was stopped once the initial roughness was no more visible. Therefore, grinding did not remove an entire layer of the coating. This means that the response to the sliding wear test was mainly demanded to the final layer of the coating, which should have experienced the same amount of peening irrespective of the total thickness. As such, it is likely that peening was not a major factor in explaining the slightly better sliding wear resistance of the thicker coatings. The role of peening (or absence thereof) can also be interpreted with reference to the literature. Torkashvand et al. [33] studied 250 µm-thick coatings ground to various thicknesses (down to 30 µm) and 50 µm-thick coatings also ground to 30 µm, and concluded that (1) the wear resistance started to decrease a bit when a coating was ground to <150 µm, because some substrate deformation began under the chosen test

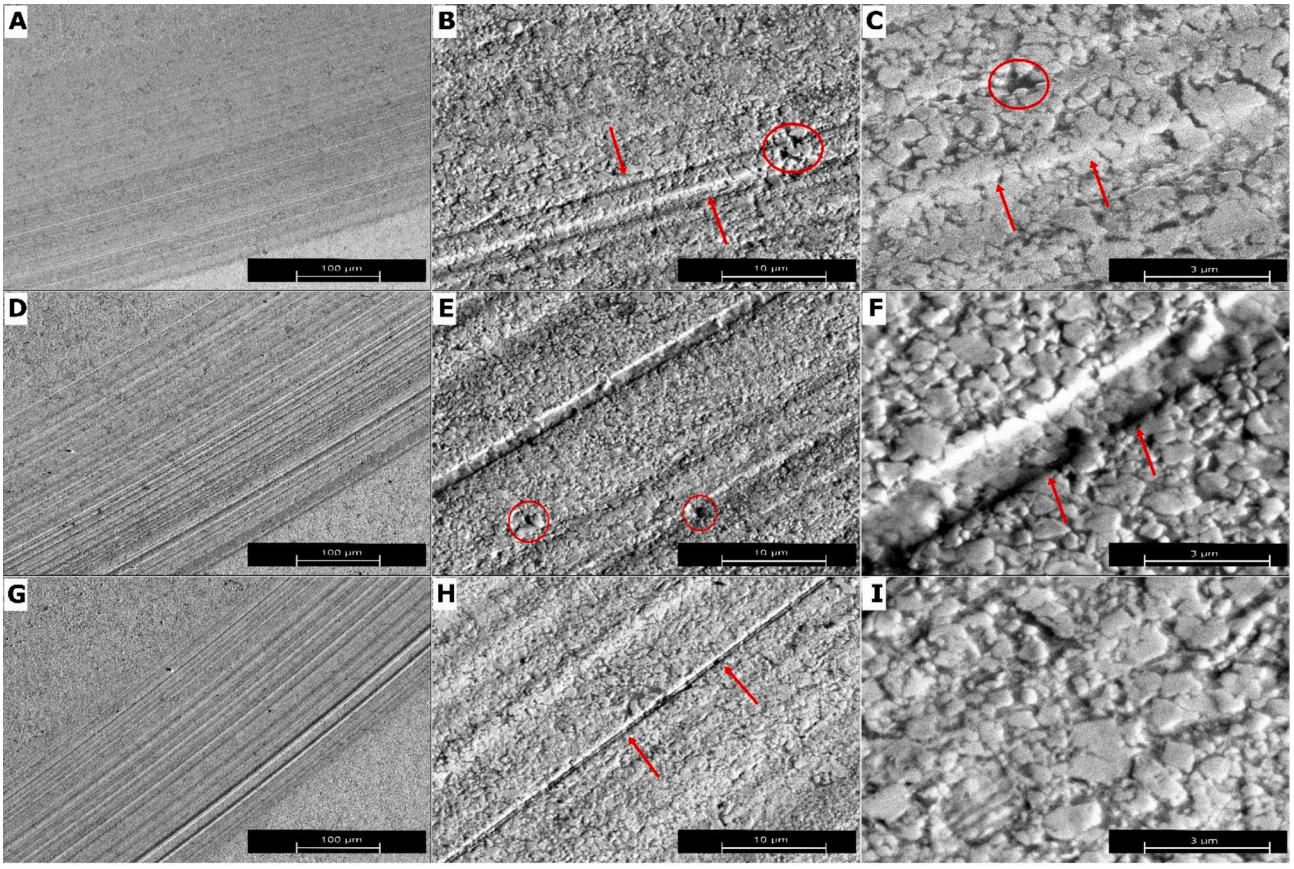

Fig. 20. SEM micrographs of the worn surfaces after ball-on-disk testing of the 150 µm-thick coatings deposited with the N3 configuration: P1 (A, B, C), P2 (D, E, F), P3 (G, H, I); arrows in panels B, C, F, H indicate shallow abrasive grooves; circles in panels B, C, E indicate pull-outs.

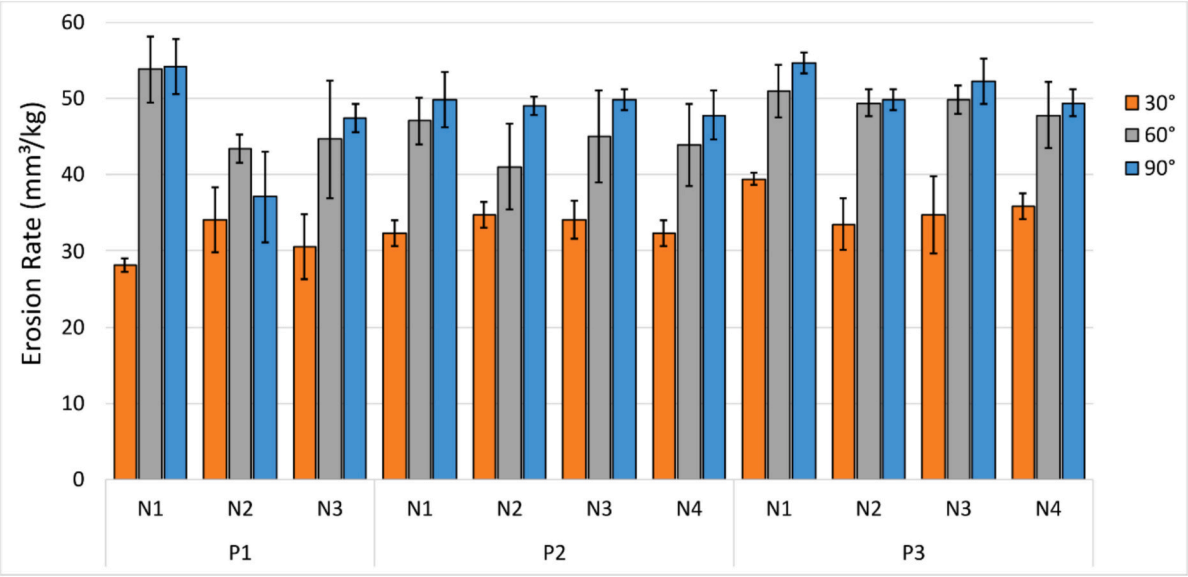

Fig. 21. Erosion rate values for the 150 µm coatings.

conditions, and that (2) there was no difference between the thick and thin coatings once they were both ground to 30 µm, although at that point, the thinned-down thick coating should have exposed layers that had been subjected to a much more intense peening action. This implied that the influence of peening was negligible compared to that of the thickness itself. Thus, in the present work, thickness can be assumed to play a major role. Indeed, the maximum sub-surface shear stress under the present test conditions can be estimated to occur at a depth of around 30 µm. With a 50 µm-thick coating (made slightly thinner by grinding and polishing), it is inferred that the steel substrate is subjected to non-negligible stresses and deforms (at least) elastically. This favors deeper penetration of the counterbody asperities into the surface and/or

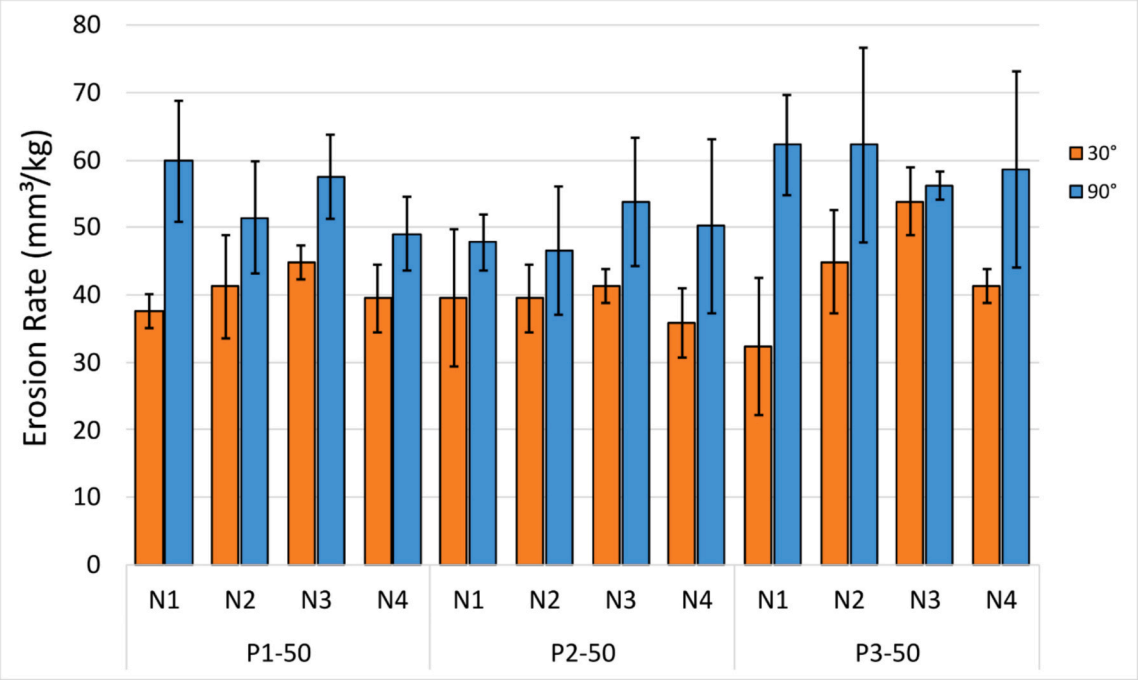

Fig. 22. Erosion rate values for the 50 μm coatings.

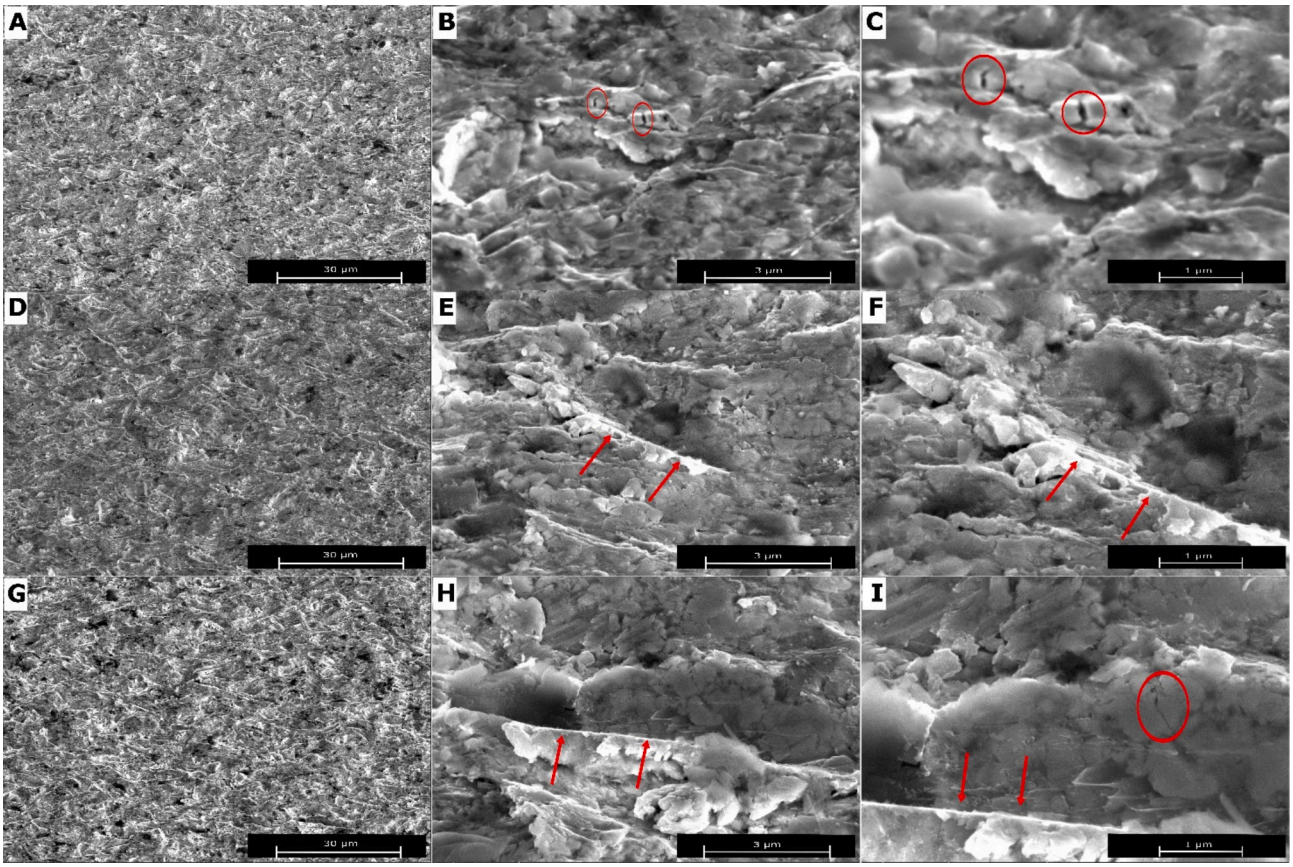

Fig. 23. SEM micrographs of the erosion scars produced on the 150 μm-thick coatings deposited with the N3 configuration at 30°: P1 (A, B, C), P2 (D, E, F), P3 (G, H, I); arrows in panels E, F, H, I indicate chipping surface; circles in panels B, C, I indicate carbide cracks.

subjects the coating to greater stresses (as a WC-CoCr coating is harder and elastically stiffer than carbon steel).

Low and high magnification SEM images of the wear tracks on the 150 μm coating surfaces, with a constant track radius ($r = 6$ mm), are presented in Fig. 19 and Fig. 20 for the coatings fabricated from the three feedstock powders and sprayed with nozzles N1 and N3. The

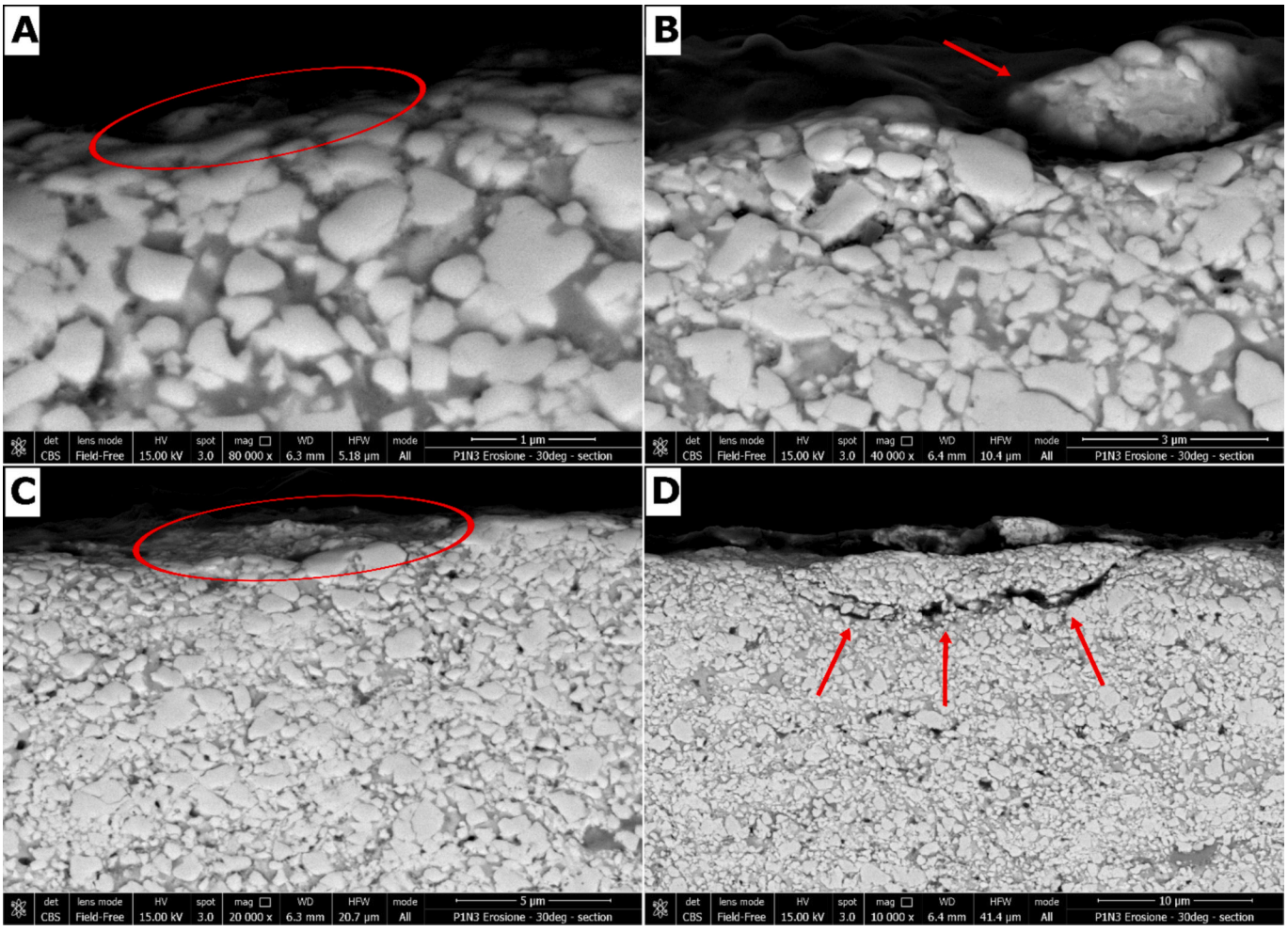

Fig. 24. Cross-sectional SEM images of the eroded surfaces of the 150 µm-thick coatings deposited with the N3 configuration coating at 30°, A) deformation of WC particles, B) chipping from the surface, C) shallow groove, D) subsurface cracks.

primary wear mechanisms identified from SEM analysis involve carbide pull-outs, resulting in pit formation, and abrasion, with varying degrees of significance among the coatings. Additionally, carbide cracks were observed in P1N1 as indicated by arrows. The wear behavior of thermal spray WC-based coatings is typically influenced by two key factors: test conditions and the inherent tribological characteristics of the coating. As the test conditions become more severe, the material removal mechanism can transition from carbide pull-out to plowed grooves, and eventually, significant cracking and delamination of whole splats, resulting in pit formation on the surface [39]. Additionally, brittle phases within the coating can affect its degradation by facilitating crack initiation and propagation. In coatings with brittle phases, surface and/or subsurface cracking can take place through the brittle phase, leading to the spallation of whole splats. However, the brittleness issue can be mitigated by reducing the flame temperature using the HVAF process. By eliminating brittle phases, the wear mechanism can be confined to carbide pull-outs and grooving, as seen in these samples, thereby enhancing the coating's performance [40].

In the N1 condition, when coupling the worn surface morphologies with the corresponding specific wear rate values, it is evident that samples with more numerous and deeper grooves correspond to higher specific wear rates (e.g., P2N1: Fig. 19 D-F). On the other hand, the grooves in P2N3 (Fig. 20 D-F) are deeper, larger, and more numerous compared to samples P1N3 and P3N3, but with almost no signs of carbide pull-outs, and specific wear rates do not differ among these three samples.

Abrasive grooves could have formed because of repeated sliding of the alumina ball over the surface, causing the coating material to be pushed laterally according to a plowing mechanism [41]. Trapped debris probably also contributed. Another notable difference between the two examined configurations is the presence of pits within the wear track of the N1 samples (Fig. 19), which are more pronounced than those in the N3 specimens (Fig. 20). These pits may have formed due to the lower cohesion of the coatings, influenced by different hardware configuration parameters. The presence of these pits can facilitate the process of material removal. However, the pits are not reflected in the measured volume loss, as they can be filled with wear products. Therefore, despite the greater number of pits in the P1N1 sample, its specific wear rate was found to be lower than that of P2N1. Likewise, there is no systematic difference between the N1- and N3-series of samples despite the greater number of pits on the former.

3.6. Erosion resistance

As depicted in Fig. 21 and Fig. 22, the overlapping error bars (indicating standard deviation) indicate that all the erosion rate results obtained at the 60° and 90° impingement angles are almost indistinguishable from one another. This means that the coatings are not much sensitive to the impingement angle within this range, and it also suggests that the influence of the powder and nozzle configurations employed is negligible. However, erosion rates under an impingement angle of 30° are, in most cases, lower. This means that the erosion

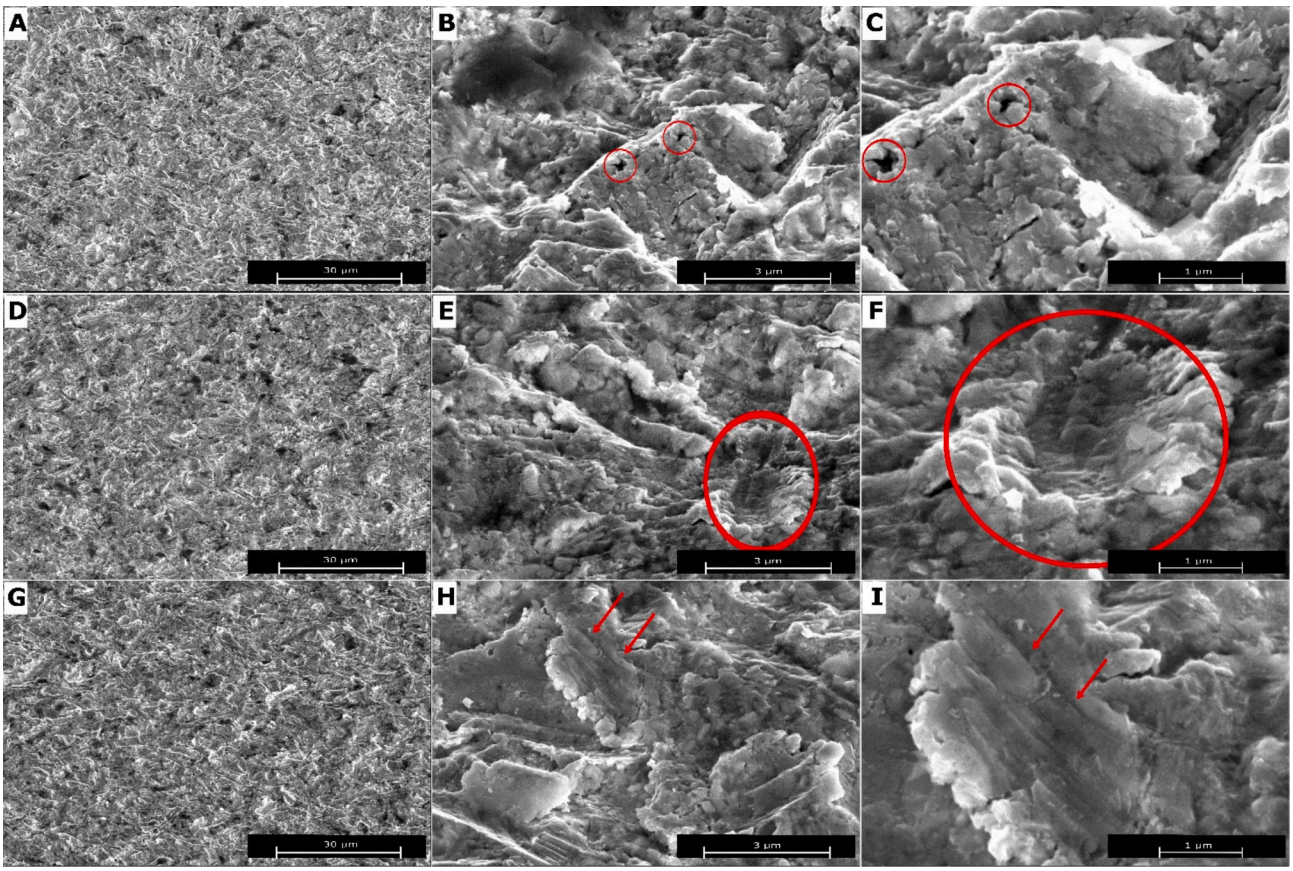

Fig. 25. SEM micrographs of the erosion scars produced on the 150 µm-thick coatings deposited with the N3 configuration at 60°: P1 (A, B, C), P2 (D, E, F), P3 (G, H, I); arrows in panels H, I indicate chipping surface; circles in panels B, C indicate carbide pull-outs; circles in panels E, F indicate plowing.

response of the coatings is more akin to that of brittle materials, although their behavior is not fully brittle, in light of the absence of a further increase from 60° to 90°. Moreover, although the tests done on the 150 µm and 50 µm coatings had a different duration, it can be concluded that, in most cases, the erosion rate values for the thinner coatings are slightly higher than those for the thicker coatings, which can possibly be ascribed, once again, to the greater penetration afforded by the deformation of the substrate.

SEM micrographs at three different magnifications (4000×, 40,000×, and 80,000×) in Fig. 23 show the surface morphology of the erosion scars at a 30° impingement angle for coatings sprayed with the N3 configuration. The main erosion wear mechanism observed in P1, P2 and P3 coatings is ductile abrasion, which results in micro-cutting (chipping) and/or micro-plowing, as indicated by the visible "lips" of material lifted along the sides of the grooves (see arrows). Micro-cracks, carbide fracturing and pull-outs (circles) along those "lips" are the result of the extensive and repeated plastic deformation phenomena during grooving, coupled with the limited deformability of the cermet. As a result, small fragments of material are progressively removed.

Cross-sectional SEM micrographs provide a better understanding of the erosive wear mechanism. In Fig. 24A, the erodent particles cut through the WC grains. Additionally, Fig. 24B shows that abrasive particles remove a segment of the coating material through larger-scale chipping upon collision with the surface. Fig. 24C reveals a surface groove caused by a particle that displaced the matrix and the carbides. Another erosion wear scenario proposed by Li et al. [42] involves the creation and interlinking of subsurface cracks that contribute to material removal, in addition to the surface evolution mechanisms. They conducted erosion tests on conventional WC-CoCr coatings with varying porosities applied using HVOF and HVAF processes, at different impact angles. They suggest that crack nucleation and propagation in dense coatings can be attributed to cracks formed in weak regions and stress concentration areas. Material removal can occur as these fissures connect and propagate towards the surface. This mechanism can be seen in Fig. 24D.

For the tests conducted at a 60° impingement angle on coatings sprayed with the N3 configuration, SEM images at low and high magnification (Fig. 25) reveal that plowing and cutting (chipping), together with small pits due to the pull-out of fractured carbides, are still the main wear mechanisms. Compared to the 30°-tests, however, the grooves caused by plowing and cutting are shorter and deeper, consistent with the greater penetration depths of erosive particles impacting at a higher incidence angle. At the same time, chipping and carbide pull-out along the lips are more numerous. At a 90° impingement angle (Fig. 26), the particles indent the surface at or close to normal incidence, resulting in the deepest penetration, with more frequent signs of cracking and carbide pull-out.

Thus, in spite of the presence of signs of ductile abrasion mechanisms, the limited plastic deformability of the hardmetal, which readily results in the propagation of cracks, justifies the observation of higher erosion rates at 60° and 90°, which is more typical of brittle materials, as noted previously.

4. Conclusions

This study compared the HVAF deposition of three different types of WC-CoCr feedstock powders: a rounded, porous one obtained by agglomeration and sintering (P1); a dense and angular one obtained by sintering and crushing (P2); and one with intermediate features (P3). All powders were sprayed under four different nozzle configurations to investigate the microstructure of the resulting coatings and their mechanical and tribological behavior. The main findings are as follows:

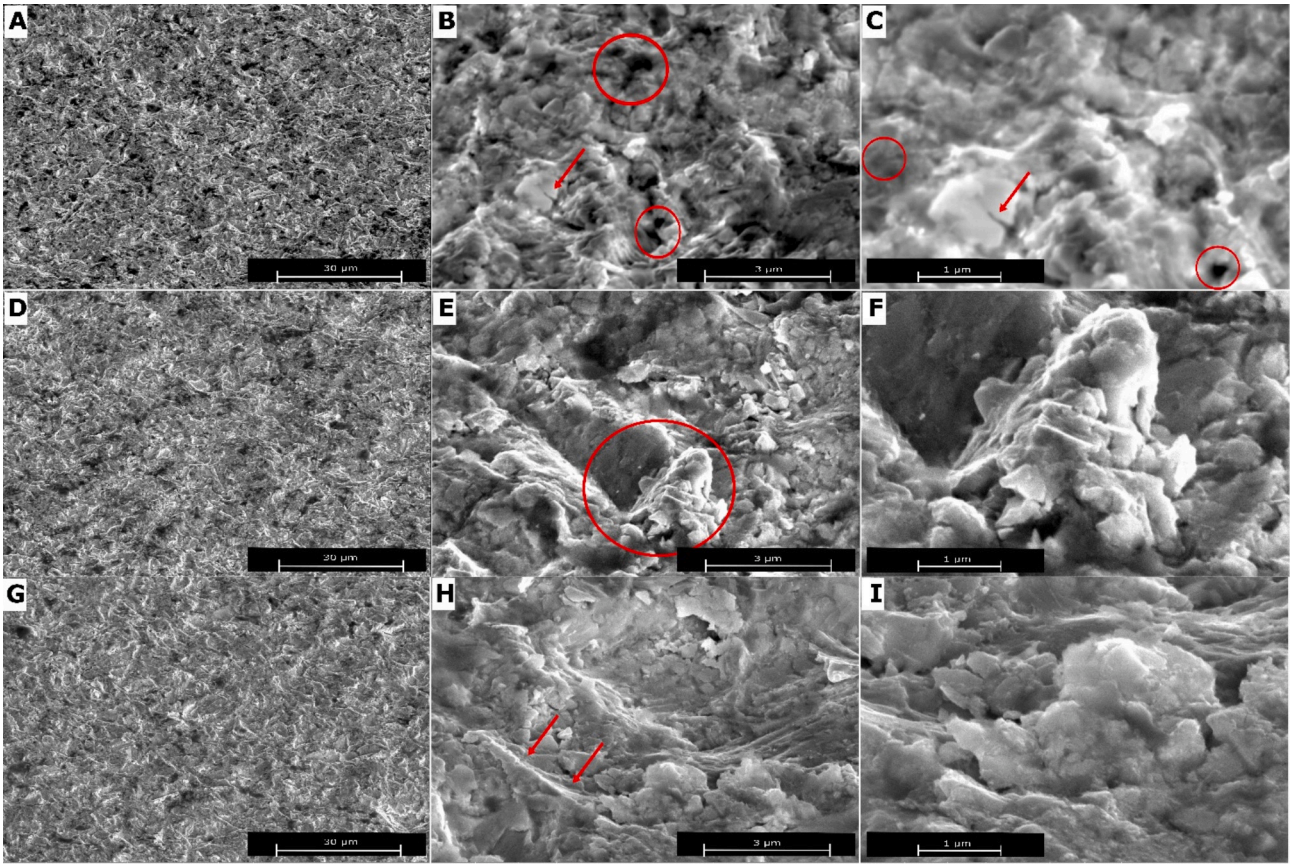

Fig. 26. SEM micrographs of the erosion scars produced on the 150 µm-thick coatings deposited with the N3 configuration at 90°: P1 (A, B, C), P2 (D, E, F), P3 (G, H, I); arrows in panel H indicate chipping of the surface; circles in panels B, C indicate carbide pull-outs; the circle in panel E indicates ductile indentation.

- The deposition rate of the P1 and P2 powders decreased as the nozzle configuration was changed in such a way that the particles' impact velocity was increased, i.e. with increasing exit diameter and when changing from a configuration with no secondary air-fuel combustion in the nozzle to one with secondary combustion. This result is clearly ascribed to increased rebounding.

  Interestingly, the porous P1 powder had marginally lower deposition rates than the dense P1 one. On the other hand, the deposition rate of the P3 powder was much less sensitive to the nozzle configuration and, under configurations that promote high impact velocity, it was higher than for the other powders.
- The microhardness of the coatings, by contrast, increased systematically when changing the nozzle configuration to produce higher impact velocity, which is ascribed to stronger interparticle cohesion and stronger peening effects.

  On the other hand, the powder type had little influence on the microhardness of the coatings.

  It was also noted that 50 µm-thick coatings were softer than the corresponding 150 µm-thick ones deposited under the same conditions but with a greater number of torch passes. It is however, not clear to what extent this was a "real" effect due to the more intense peening exerted on the thicker coatings, and to what extent it was an artefact due to the indentation diagonals being close to the coating thickness (i.e. an influence from the substrate and the mounting resin cannot be ruled out).
- XRD analysis of feedstock powders showed similar phases with minor differences, such as narrower peaks in the S&C feedstock. XRD analysis of the coatings confirmed HVAF's effectiveness in limiting decarburization and oxidation, as the intensity of the diffraction peaks of decarburized phases (W_2C, W) was low.
- All coatings exhibited excellent sliding wear resistance against Al_2O_3, with specific wear in the order of 10^{-8} $mm^3/(N•m)$. There was no significant difference among the coatings, regardless of the feedstock powder and nozzle configuration. The only truly influential factor was the thickness of the coating: thinner coatings generally showed higher wear rates compared to thicker coatings under sliding wear conditions. This was ascribed primarily to the greater deformation of the thin coatings: the contact stress distribution affected the substrate, causing it to bend under load and promoting deeper penetration of abrasive asperities in the sample. The main wear mechanisms observed during sliding wear tests were pitting and abrasive grooving, with their respective incidence changing somewhat depending on the nozzle configuration, although this did not result in measurable differences among the specific wear rates.
- The influence of powders and nozzle configurations on the dry erosion resistance was negligible, but coatings generally experienced higher erosion rates at 90° and 60° impact angles compared to 30°. Three common wear mechanisms, including pitting, plowing, and chipping, were observed on the surfaces. Deeper plows and indents at 60° and 90° incidence promoted the chipping of the extruded lips of material, explaining the greater erosion rate. Thicker coatings also exhibited better performance under erosive wear conditions, again probably because deformation of the substrate under the thin coating allowed deeper penetration of the abrasives.

The study provides valuable insights into the performance and characteristics of WC-CoCr coatings sprayed using different feedstock powders and HVAF deposition techniques. The proper choice of feedstock powders and optimization of deposition parameters can lead to improved hardness and deposition rate. In particular, the results highlight that the newly developed powder offers notable advantages, such

as higher deposition efficiency, which accelerates the spraying process and boosts production productivity, along with reduced sensitivity to parameter variations. These benefits are achieved while maintaining coating properties comparable to those obtained with the other powders.

CRediT authorship contribution statement

L. Bortolotti: Writing – original draft, Methodology, Investigation, Formal analysis, Data curation. **G. Ruggiero:** Methodology, Investigation, Formal analysis. **G. Bolelli:** Writing – review & editing, Methodology, Investigation, Conceptualization. **L. Lusvarghi:** Writing – review & editing, Supervision, Methodology, Conceptualization. **S. Morelli:** Writing – review & editing, Methodology, Investigation. **S. Björklund:** Writing – review & editing, Methodology, Conceptualization. **O. Lanz:** Writing – review & editing, Resources, Conceptualization. **S. Joshi:** Writing – review & editing, Supervision, Resources, Methodology, Data curation, Conceptualization.

Declaration of competing interest

The authors declare the following financial interests/personal relationships which may be considered as potential competing interests: O. Lanz reports a relationship with Höganäs Germany GmbH, Säckinger Str. 51, Laufenburg, Germany that includes: employment. If there are other authors, they declare that they have no known competing financial interests or personal relationships that could have appeared to influence the work reported in this paper.

Acknowledgments

The authors would like to thank Höganäs for supplying the feedstock powders for this study. Thanks to Dr. Miriam Hanuskova (Department of Engineering "Enzo Ferrari", University of Modena and Reggio Emilia, Italy) for performing the particle size distribution analyses.

Data availability

Data will be made available on request.

References

[1] E. Lassner, W.-D. Schubert, Tungsten, 1999, https://doi.org/10.1007/978-1-4615-4907-9.
[2] Kinson J, Mullet C, Scott W, "© 2000 ASM international. All rights reserved. ASM Specialty Handbook: Nickel, Cobalt, and Their Alloys (#06178G) www.asminternational.org," 2000.
[3] J.M. Perry, A. Neville, T. Hodgkiess, A comparison of the corrosion behavior of WC-co-Cr and WC-co HVOF thermally sprayed coatings by in situ atomic force microscopy (AFM), J. Therm. Spray Technol. 11 (4) (2002) 536–541, https://doi.org/10.1361/105996302770348673/METRICS.
[4] L.M. Berger, Application of hardmetals as thermal spray coatings, Int. J. Refract. Met. Hard Mater. 49 (1) (2015) 350–364, https://doi.org/10.1016/J.IJRMHM.2014.09.029.
[5] V. Matikainen, H. Koivuluoto, P. Vuoristo, A study of Cr_3C_2-based HVOF- and HVAF-sprayed coatings: abrasion, dry particle erosion and cavitation erosion resistance, Wear 446–447 (2020) 203188, https://doi.org/10.1016/j.wear.2020.203188.
[6] L. Janka, et al., Improving the high temperature abrasion resistance of thermally sprayed Cr3C2-NiCr coatings by WC addition, Surf. Coat. Technol. 337 (2018) 296–305, https://doi.org/10.1016/J.SURFCOAT.2018.01.035.
[7] G. Bolelli, L. M. Berger, M. Bonetti, and L. Lusvarghi, "Comparative study of the dry sliding wear behaviour of HVOF-sprayed WC-(W,Cr)2C-Ni and WC-CoCr hardmetal coatings," Wear, vol. 309, no. 1–2, pp. 96–111, Jan. 2014, doi:https://doi.org/10.1016/J.WEAR.2013.11.001.
[8] L.-M. Berger, S. Saaro, T. Naumann, M. Kašparova, F. Zahálka, Microstructure and Properties of HVOF-Sprayed WC-(W,Cr)2C-Ni Coatings, J. Therm. Spray Technol. 17 (3) (2008) 395–403, https://doi.org/10.1007/s11666-008-9189-x.
[9] L. M. Berger, S. Saaro, T. Naumann, M. Kašparova, and F. Zahálka, "Influence of feedstock powder characteristics and spray processes on microstructure and properties of WC-(W,Cr)2C-Ni hardmetal coatings," Surf. Coat. Technol., vol. 205, no. 4, pp. 1080–1087, 2010, doi:https://doi.org/10.1016/j.surfcoat.2010.07.032.
[10] H.J. Kim, Y.G. Kweon, R.W. Chang, Wear and erosion behavior of plasma-sprayed WC-co coatings, J. Therm. Spray Technol. 3 (2) (1994) 169–178, https://doi.org/10.1007/BF02648274/METRICS.
[11] J.K.N. Murthy, B. Venkataraman, Abrasive wear behaviour of WC–CoCr and Cr3C2–20(NiCr) deposited by HVOF and detonation spray processes, Surf. Coat. Technol. 8 (200) (2006) 2642–2652, https://doi.org/10.1016/J.SURFCOAT.2004.10.136.
[12] L. Jacobs, M.M. Hyland, M. De Bonte, Study of the influence of microstructural properties on the sliding-wear behavior of HVOF and HVAF sprayed WC-cermet coatings, J. Therm. Spray Technol. 1 (8) (1999) 125–132, https://doi.org/10.1361/105996399770350656.
[13] G. Bolelli, et al., Tribology of HVOF- and HVAF-sprayed WC–10Co4Cr hardmetal coatings: a comparative assessment, Surf. Coat. Technol. 265 (2015) 125–144, https://doi.org/10.1016/J.SURFCOAT.2015.01.048.
[14] K. Torkashvand, et al., Tribological behavior of HVAF-sprayed WC-based coatings with alternative binders, Surf. Coat. Technol. 436 (2022), https://doi.org/10.1016/J.SURFCOAT.2022.128296.
[15] H.L. De Villiers Lovelock, Powder/processing/structure relationships in WC-co thermal spray coatings: a review of the published literature, J. Therm. Spray Technol. 7 (3) (1998) 357–373, https://doi.org/10.1361/105996398770350846/METRICS.
[16] R. Schwetzke, H. Kreye, Microstructure and properties of tungsten carbide coatings sprayed with various high-velocity oxygen fuel spray systems, J. Therm. Spray Technol. 8 (3) (1999) 433–439, https://doi.org/10.1361/105996399770350395/METRICS.
[17] Q. Wang, S. Zhang, Y. Cheng, J. Xiang, X. Zhao, G. Yang, Wear and corrosion performance of WC-10Co4Cr coatings deposited by different HVOF and HVAF spraying processes, Surf. Coat. Technol. 218 (1) (2013) 127–136, https://doi.org/10.1016/J.SURFCOAT.2012.12.041.
[18] P. Fauchais, G. Montavon, and G. Bertrand, "From Powders to Thermally Sprayed Coatings", doi:https://doi.org/10.1007/s11666-009-9435-x.
[19] L. Pawlowski, The Science and Engineering of Thermal Spray Coatings, 2nd ed., Wiley, Chichester, UK, UK, 2008 https://doi.org/10.1002/9780470754085.
[20] S. Kamnis, S. Gu, Study of in-flight and impact dynamics of nonspherical particles from HVOF guns, J. Therm. Spray Technol. 19 (1–2) (2010) 31–41, https://doi.org/10.1007/s11666-009-9382-6.
[21] C. Lyphout *et al.*, "Tribological Properties of Hard Metal Coatings Sprayed by High-Velocity Air Fuel Process", doi:https://doi.org/10.1007/s11666-015-0285-4.
[22] C. Verdon, A. Karimi, J.L. Martin, A study of high velocity oxy-fuel thermally sprayed tungsten carbide based coatings. Part 1: microstructures, Mater. Sci. Eng. A 246 (1–2) (1998) 11–24, https://doi.org/10.1016/S0921-5093(97)00759-4.
[23] V. Matikainen, H. Koivuluoto, P. Vuoristo, J. Schubert, Š. Houdková, Effect of nozzle geometry on the microstructure and properties of HVAF-sprayed WC-10Co4Cr and Cr3C2-25NiCr coatings, J. Therm. Spray Technol. 27 (4) (2018) 680–694, https://doi.org/10.1007/s11666-018-0717-z.
[24] G. Mauer, K.-H. Rauwald, Y.J. Sohn, R. Vaßen, The potential of high-velocity air-fuel spraying (HVAF) to manufacture bond coats for thermal barrier coating systems, J. Therm. Spray Technol. 33 (2–3) (2024) 746–755, https://doi.org/10.1007/s11666-023-01659-2.
[25] P.H. Gao, Y.G. Li, C.J. Li, G.J. Yang, C.X. Li, Influence of powder porous structure on the deposition behavior of cold-sprayed WC-12Co coatings, J. Therm. Spray Technol. 17 (5–6) (2008) 742–749, https://doi.org/10.1007/s11666-008-9258-1.
[26] C.J. Li, Y.Y. Wang, G.J. Yang, A. Ohmori, K.A. Khor, Effect of solid carbide particle size on deposition behaviour, microstructure and wear performance of HVOF cermet coatings, Mater. Sci. Technol. 20 (9) (2004) 1087–1096, https://doi.org/10.1179/026708304225019722.
[27] P. Chivavibul, et al., Effect of powder characteristics on properties of warm-sprayed WC-co coatings, J. Therm. Spray Technol. 19 (1–2) (2010) 81–88, https://doi.org/10.1007/s11666-009-9438-7.
[28] V.V. Sobolev, J.M. Guilemany, Flattening of droplets and formation of splats in thermal spraying: a review of recent work - part 2, J. Therm. Spray Technol. 8 (2) (1999) 301–314, https://doi.org/10.1361/105996399770350520/METRICS.
[29] G. Bolelli, et al., Sliding and abrasive wear behaviour of HVOF- and HVAF-sprayed Cr3C2–NiCr hardmetal coatings, Wear 358–359 (2016) 32–50, https://doi.org/10.1016/J.WEAR.2016.03.034.
[30] A. Nouri, A. Sola, Powder morphology in thermal spraying, J Adv Manuf Process 1 (3) (2019) e10020, https://doi.org/10.1002/AMP2.10020.
[31] H. Wang, Y. Li, M. Gee, H. Zhang, X. Liu, X. Song, Sliding wear resistance enhancement by controlling W2C precipitation in HVOF sprayed WC-based cermet coating, Surf. Coat. Technol. 387 (2020) 125533, https://doi.org/10.1016/J.SURFCOAT.2020.125533.
[32] C. Verdon, A. Karimi, J.-L. Martin, Microstructural and analytical study of thermally sprayed WC-co coatings in connection with their wear resistance, Mater. Sci. Eng. A 234–236 (1997) 731–734, https://doi.org/10.1016/S0921-5093(97)00377-8.
[33] K. Torkashvand, M. Gupta, S. Björklund, S. Joshi, Tribological performance of thin HVAF-sprayed WC-CoCr coatings fabricated employing fine powder feedstock, J. Therm. Spray Technol. 32 (4) (2022) 1033–1046, https://doi.org/10.1007/S11666-022-01506-W/FIGURES/12.
[34] K. Kato, K. Adachi, Wear of advanced ceramics, Wear 253 (11–12) (2002) 1097–1104, https://doi.org/10.1016/S0043-1648(02)00240-5.
[35] J.A.R. Wesmann, S. Kuroda, N. Espallargas, The role of oxide Tribofilms on friction and Wear of different thermally sprayed WC-CoCr, J. Therm. Spray Technol. 26 (3) (2017) 492–502, https://doi.org/10.1007/s11666-017-0522-0.
[36] E. Rabinowicz, The Wear coefficient—magnitude, scatter, uses, J. Lubr. Technol. 103 (2) (1981) 188–193, https://doi.org/10.1115/1.3251624.

[37] Z.Y. Piao, B.S. Xu, H.D. Wang, C.H. Pu, Effects of thickness and elastic modulus on stress condition of fatigue-resistant coating under rolling contact, Journal of Central South University of Technology (English Edition) 17 (5) (2010) 899–905, https://doi.org/10.1007/S11771-010-0574-5.
[38] K. Holmberg, H. Ronkainen, A. Matthews, Tribology of thin coatings, Ceram. Int. 26 (7) (2000) 787–795, https://doi.org/10.1016/S0272-8842(00)00015-8.
[39] H. Wang, X. Wang, X. Song, X. Liu, X. Liu, Sliding wear behavior of nanostructured WC-co-Cr coatings, Appl. Surf. Sci. 355 (2015) 453–460, https://doi.org/10.1016/J.APSUSC.2015.07.144.
[40] K. Torkashvand, S. Joshi, M. Gupta, Advances in thermally sprayed WC-based Wear-resistant coatings: co-free binders, processing routes and Tribological behavior, J. Therm. Spray Technol. 31 (3) (2022) 342–377, https://doi.org/10.1007/S11666-022-01358-4/FIGURES/25.
[41] K. Kato, Micro-mechanisms of wear — wear modes, Wear 153 (1) (1992) 277–295, https://doi.org/10.1016/0043-1648(92)90274-C.
[42] Y. Li, Y. Lian, J. Cao, and L. Li, "Solid particle erosion behavior of HVOF/HVAF sprayed WC-co-Cr coatings," *doi:*10.1177/1350650115608209, vol. 230, no. 6, pp. 634–643,Sep. 2015, doi:https://doi.org/10.1177/1350650115608209.